

Department of Physics and Astronomy

University of Heidelberg

Bachelor Thesis in Physics

submitted by

Hannah Klingenmeyer

born in Heidelberg

2015

**Optimisation of the Local On-line Tracking
for Triggering with the Transition Radiation Detector
in A Large Ion Collider Experiment
at the Large Hadron Collider**

This bachelor thesis has been carried out by Hannah Klingenmeyer

at the

Physikalisches Institut at the University of Heidelberg

under the supervision of

Prof. Dr. Johanna Stachel

Abstract

The Transition Radiation Detector at the LHC (CERN) provides electron identification in the central barrel of ALICE as well as trigger contributions for electrons and jets. More than 65,000 multi-chip modules allow a fast on-detector reconstruction of chamber-wise track segments, which include position, angle and PID information. These tracklets are then merged into tracks which provide information on transverse momenta and electron identification.

This thesis focuses on the optimisation of the local on-line tracking in the multi-chip modules by using Monte Carlo simulations of minimum bias pp collisions at 8 TeV. The rejection of multiple tracklets in order to improve the PID performance is implemented in the simulation of the front-end electronics. Furthermore, the algorithm of the straight-line fit defining the tracklets is optimised by introducing corrections to the transverse position and the deflection of the tracklets. A method to correct the mis-alignment of the detector modules in the MCMs is implemented and tested.

Additionally, the participation in the commissioning of the TRD for Run 2 during the time of this thesis is presented. This particularly included the testing of different supermodules both prior to and after the installation in the detector.

Zusammenfassung

Der Übergangstrahlungsdetektor am LHC (CERN) ermöglicht die Identifikation von Elektronen im Zentralbereich des ALICE-Experiments und liefert Elektronen- und Jet-Trigger. Durch mehr als 65 000 Multi-Chip-Module wird eine schnelle Rekonstruktion der Spursegmente für jede Kammer noch vor Auslese des Detektors erreicht. Diese Spursegmente enthalten Informationen zu Position, Winkel und Identität der Teilchen und werden zu vollständigen Spuren zusammengefügt, die Aufschluss über den Transversalimpuls sowie die Elektronenwahrscheinlichkeit der Teilchen geben.

In dieser Arbeit wird die lokale Spurrekonstruktion in den Multi-Chip-Modulen mit Hilfe von Monte Carlo-Simulationen von 8 TeV pp-Kollisionen bei minimalem Untergrund optimiert. Mehrfach gefundene Spursegmente werden in der Simulation der Front-End-Elektronik ausgeschlossen, um die Teilchenidentifikation zu verbessern. Des Weiteren wird der Algorithmus der linearen Anpassung, die die Spursegmente definiert, durch Einführung von Korrekturen der transversalen Position und der Ablenkung der Spursegmente optimiert. Außerdem wird eine Methode auf den Multi-Chip-Modulen implementiert und getestet, die die Verschiebung der Detektormodule ausgleicht.

Zusätzlich wird der Beitrag zur Inbetriebnahme des Übergangstrahlungsdetektors für die zweite Betriebsphase des LHC, der während dieser Arbeit geleistet wurde, erläutert. Dieser beinhaltete insbesondere das Testen verschiedener Supermodule sowohl vor als auch nach deren Einbau in den Detektor.

Contents

1	Introduction	1
1.1	Physics background	1
1.2	The Large Hadron Collider	2
1.3	A Large Ion Collider Experiment	2
1.4	Outline	4
2	The Transition Radiation Detector	5
2.1	Electron identification with transition radiation	5
2.2	Layout of the TRD	5
2.3	Principle of operation	6
2.3.1	Read-out chambers	6
2.3.2	Front-end electronics	8
2.3.3	On-line tracking	8
2.4	Triggering with the TRD	9
2.4.1	The ALICE trigger system	9
2.4.2	The TRD trigger system	9
2.5	Commissioning for Run 2	10
3	Local on-line tracking in the TRD	13
3.1	Local coordinate system	13
3.2	Tracklet calculation and tracking procedure	13
3.2.1	Signal filtering and digitization	13
3.2.2	Tracklet calculation in the TRAP	14
3.2.3	Position and deflection corrections	15
3.3	Tracklet simulation	17
4	Optimisation of the local on-line tracking	19
4.1	General procedure	19
4.2	Tracklet selection	19
4.3	Drift velocity	23
4.4	Position correction	26
4.5	Correction of mis-alignment	29
5	Summary and outlook	33

1 Introduction

Probing the fundamental structure of the universe is the goal of today's experimental particle physics. With the discovery of the Higgs boson in 2012 at CERN the existence of all fundamental particles predicted by the Standard Model of particle physics has been experimentally verified [1]. However, many unsolved questions still remain: Why is there more matter than anti-matter in the universe? What is Dark Matter made of? How can the gravitational interaction be included in the Standard Model?

Some of the largest and most complex machines ever built address these questions by observing the collisions of subatomic particles at very high energies. Accelerators are used to boost beams of particles to the required energies of several TeV, while detectors examine the collisions and record the results. Even though both accelerators and detectors are quite far advanced and provide important results, improvements of individual components can still be made. One example for such an improvement is the optimisation of the local on-line tracking in the Transition Radiation Detector of the ALICE detector at CERN, which is addressed in this thesis.

The purpose of this chapter is to provide an understanding of the background of this thesis, starting from the physics that is of interest and arriving at the experiment which houses the detector concerned in this thesis.

In the first section 1.1, the Standard Model of particle physics and the physics of heavy-ion collisions are briefly explained. The goal to explore and understand these motivates the construction of enormous particle colliders, such as the Large Hadron Collider (LHC) at CERN, Geneva (see Section 1.2), and experiments like A Large Ion Collider Experiment (ALICE, see Section 1.3) that examine such collisions to extract physical results. One of the detectors in ALICE is the Transition Radiation Detector, which is discussed in this thesis. Before it is explained in more detail in the following chapter, Section 1.4 provides a short outline of this thesis.

1.1 Physics background

The Standard Model of particle physics is a quantum field theory describing the fundamental particles of physics and their interactions, excluding the gravitational interaction [2]. The Standard Model has not yet been disproven, but on the other hand, it is by no means complete. Many phenomena, such as the existence of Dark Matter or the asymmetry of matter and anti-matter in the universe, are only partially explained, if at all. Therefore, it is of great interest to test the predictions made by, and find the limitations of the Standard Model.

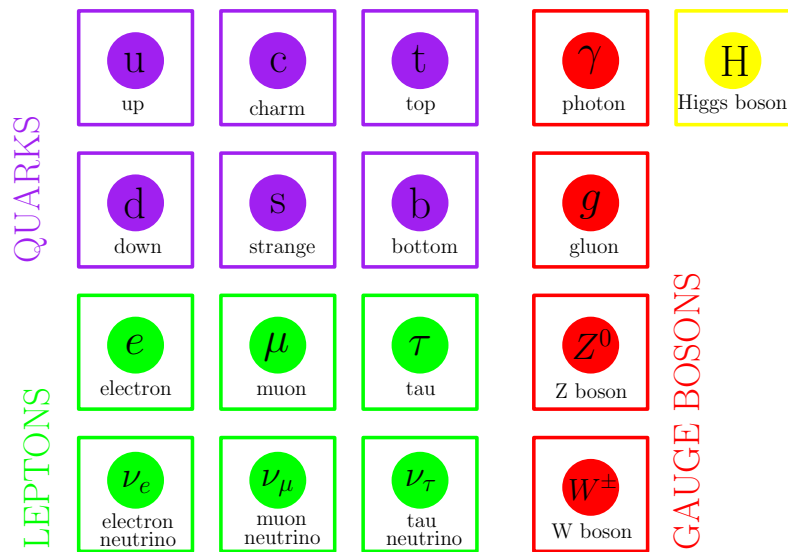


Figure 1.1: The Standard Model of Particle Physics. The fundamental particles consist of three generations of quarks and leptons as well as the four gauge bosons and the Higgs boson [2].

The elementary particles, shown in Figure 1.1, can be sorted into three groups based on their spin: The fermions with a spin of $\frac{1}{2}$ are the basic constituents of matter, the gauge bosons with a spin of 1 mediate the fundamental interactions, and the Higgs boson with a spin of 0 gives the particles their mass. The fermions can again be divided into quarks and leptons, based on the interactions they partake in. All leptons participate in the weak interaction, mediated either by a W^\pm or a Z boson, and electron, muon and tau additionally partake in the electromagnetic interaction mediated by photons. Quarks, on the other hand, participate in the strong interaction mediated by gluons, as well as in the electromagnetic and weak interactions. They are bound together by the strong force into protons, neutrons and other particles like pions, kaons etc., and are not found to exist on their own. However, there is a state predicted to have existed very shortly after the big bang, where quarks and gluons were bound only weakly at extremely high temperature, density, or both [3]. This so-called Quark Gluon Plasma (QGP) can be created in today's particle colliders like the LHC by colliding heavy nuclei at high energies, thus generating both the high temperature and density needed for the QGP. It can be used for a closer study of the interaction and properties of strongly interacting particles, as done for example in ALICE [4].

1.2 The Large Hadron Collider

The Large Hadron Collider (LHC) [5] at the European Organization for Nuclear Research (CERN) in Geneva is a particle accelerator and collider with a circumference of 26.7 km, located between Lake Geneva and the Jura mountains. Installed in the tunnel originally built for its predecessor, the Large Electron-Positron Collider (LEP), 100 metres beneath the Franco-Swiss border, it is designed to collide beams of protons or lead ions at a centre of mass energy of $\sqrt{s} = 14$ TeV (for pp collisions) and $\sqrt{s} = 5.5$ TeV (for Pb-Pb collisions) per nucleon-nucleon pair. Since operation started on 10 September 2008 until the end of the first running period in 2013, energies of $\sqrt{s} = 8$ TeV for pp collisions as well as $\sqrt{s} = 2.76$ TeV per nucleon-nucleon pair for Pb-Pb collisions have been reached, while additionally p-Pb and Pb-p collisions at $\sqrt{s} = 5.02$ TeV have taken place [6].

To keep the particles on their circular trajectory in the ring, a magnetic field of $B \approx 8.33$ T is needed for a target beam energy of 7 TeV, which in turn requires the use of superconducting magnets. Therefore, a total of 1232 installed dipole magnets are cooled down with superfluid helium to an operating temperature of 1.9 K.

In order to reach the required energies, the particles are accelerated sequentially in a series of pre-accelerators as shown in Figure 1.2, before being injected in opposite directions into the ring. The beams are then collided at four interaction points (IP) around which the four major experiments at the LHC are built [3, 5].

ATLAS (A Torroidal LHC Apparatus) and **CMS** (Compact Muon Solenoid) are general purpose detectors located at IP 1 and IP 5, respectively. Designed for similar scientific goals such as studying the Standard Model and searching for new physics, e.g. supersymmetric particles, extra dimensions or dark matter candidates, both experiments discovered the Higgs boson in 2012. The **LHCb** (Large Hadron Collider beauty) experiment, installed at IP 8, is specialised in investigating heavy-flavour physics, for example studying CP violation in the decay of B mesons, and the asymmetry of matter and antimatter observed in the universe.

As opposed to ATLAS, CMS and LHCb, which primarily use pp collisions in their physics programme, **ALICE** (A Large Ion Collider Experiment) is designed to specifically focus on heavy-ion collisions. It is located at IP 2 and will be explained more closely in the following section.

In addition to these four experiments, three smaller experiments **TOTEM**, **LHCf** and **MOEDAL** are installed at the LHC [3].

1.3 A Large Ion Collider Experiment

A Large Ion Collider Experiment (ALICE) is the dedicated heavy-ion experiment at the CERN LHC. Its main purpose is to study strongly interacting matter and to search for the QGP (see Section 1.1) by observing the high-multiplicity events of Pb-Pb collisions at a design centre of mass energy of $\sqrt{s_{NN}} = 5.5$ TeV. The experiment has an overall size of $16 \times 16 \times 26$ m³ with a total weight of $\sim 10\,000$ t and comprises several detector systems, shown in Figure 1.3.

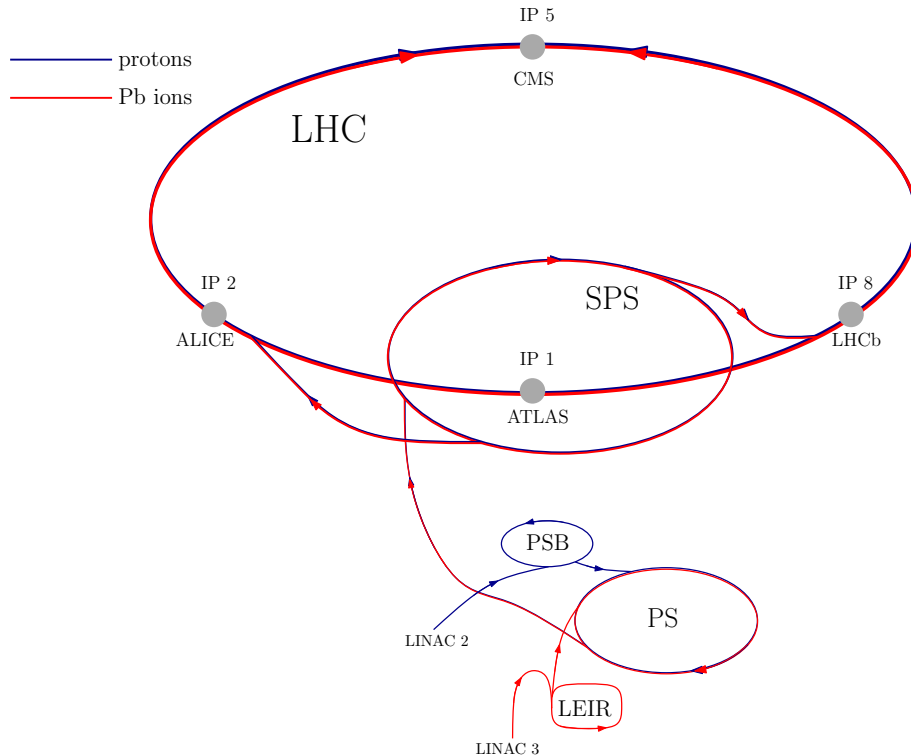


Figure 1.2: Overview of the LHC and its pre-accelerators (adapted from [7]). After the protons are accelerated in the linear accelerator LINAC2, they are transferred subsequently to the Proton Synchrotron Booster (PSB), the Proton Synchrotron (PS) and the Super Proton Synchrotron (SPS), before being injected into the LHC. The Pb ions are first accelerated in LINAC3 and the Low Energy Ion Ring (LEIR) before being transferred to the PS and SPS as well. The beams are injected into the LHC in clockwise and anti-clockwise direction, and brought to collision at four Interaction Points (IP), where the four major experiments are located.

The central barrel detectors are located inside the solenoid magnet, which provides a longitudinal magnetic field of $B = 0.5$ T. From the interaction point outwards, the Inner Tracking System (ITS), the Time Projection Chamber (TPC), the Transition Radiation Detector (TRD), and the Time Of Flight (TOF) are installed in a steel support structure called the spaceframe. They cover the full azimuth with an 18-fold segmentation, and a range in pseudo-rapidity of $|\eta| \leq 0.9$.

The TPC, located between $r = 85$ cm and $r = 247$ cm, is used as the main tracking device of ALICE [6]. It consists of a 90 m^3 cylinder filled with a Ne-CO₂ mixture, which is operated as a drift chamber and read out by multi-wire proportional chambers at the end plates. This allows for Particle IDentification (PID) by measuring the specific energy loss $-\frac{dE}{dx}$ of a particle traversing the TPC. The ITS is sub-divided into Silicon Pixel (SPD), Silicon Strip (SSD) and Silicon Drift Detectors (SDD), consisting of two layers each. Their purpose is to provide the tracking for particles with low transverse momenta, and to improve the resolution of the tracking close to the primary vertex. Additionally, the SPD can be used for triggering. The TRD, which allows for electron identification of particles with $p_{\perp} \geq 1$ GeV/ c and can be used for tracking and triggering as well, is explained in more detail in Chapter 2. The precise time measurement by TOF allows for additional particle identification.

In the cylindrical space outside of TOF, two electromagnetic calorimeters, the PHOTon Spectrometer (PHOS) and the ElectroMagnetic Calorimeter (EMCal), along with the High Momentum Particle Identification Detector (HMPID) used for additional hadron identification up to high momenta are installed at different angular positions (see Figure 1.3).

The central barrel detectors are supplemented in forward direction by a set of detectors which are used for triggering and global event characterisation [8]. The V0 detector is made up of two arrays of scintillator counters, which are installed on each side of the interaction point. It is mainly used to estimate the centrality and event plane in Pb-Pb collisions, and provides minimum bias triggers for the central barrel detectors. The quartz Cherenkov detector T0 provides accurate time measurements and

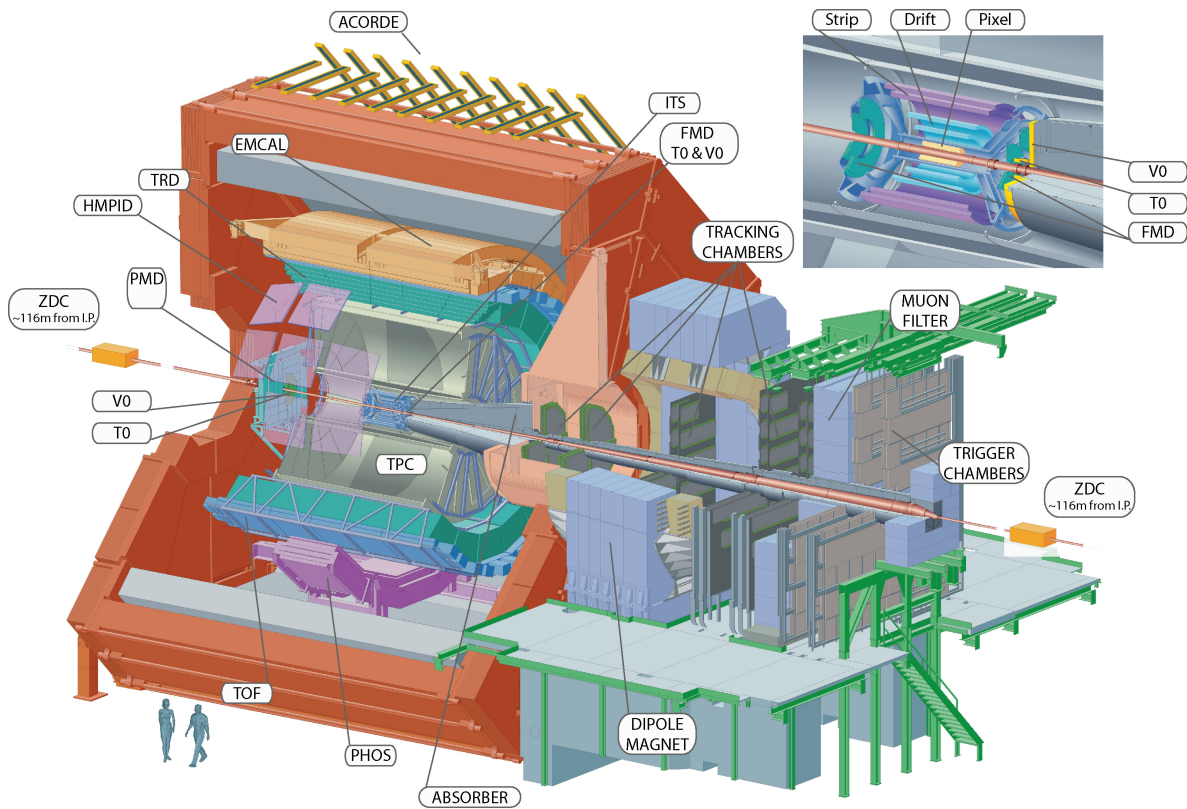


Figure 1.3: Set-up of the ALICE detector [4]: The large solenoid magnet houses the detectors of the central barrel. On the right side the muon arm with the smaller dipole magnet is shown.

can be used as a minimum bias trigger as well. Besides several other forward detectors a large muon arm equipped with a dipole magnet and several tracking chambers is installed in forward direction.

1.4 Outline

As a thorough understanding of the Transition Radiation Detector is essential for the discussion of the local on-line tracking in later chapters, the purpose of Chapter 2 is to provide a detailed description of the detector. Consequently, Sections 2.2 to 2.4 focus on the working principle of the TRD as well as its use as a trigger detector. Section 2.5 gives a short overview over the commissioning of the TRD for Run 2, and my personal involvement over the course of this thesis.

With the provided information concerning the detector, the focus can be shifted to the local on-line tracking in the TRD. This is done in Chapter 3, starting with a short description of the local coordinate system in Section 3.1. A more detailed explanation of the tracklet calculation is given in Section 3.2, while Section 3.3 gives a short overview of the tracklet simulation.

Chapter 4 comprises the main topic of this thesis, i.e. the optimisation of the local on-line tracking based on Monte Carlo simulations to improve the trigger performance of the TRD. Section 4.1 illustrates the general approach of producing Monte Carlo simulations and comparing the Monte Carlo truth to the simulated detector response by implementing an off-line analysis task. The subsequent sections all focus on the improvement of different quantities that are of importance for the local on-line tracking: Section 4.2 is concerned with the deterioration of the PID by multiple tracklets, while Sections 4.3 and 4.4 discuss the tracking parameters in detail. The last section of this chapter, Section 4.5, deals with the correction of the chamber-wise mis-alignment in the TRD.

Finally, Chapter 5 concludes this thesis after a brief summary of the work done by giving a short outlook on possible developments for the future.

2 The Transition Radiation Detector

The Transition Radiation Detector (TRD) [9] is one of the detector systems of ALICE, located in the central barrel inside the solenoid magnet (see Figure 1.3). Besides the reconstruction of the particle track through the detector, one purpose of the TRD is to provide electron identification for charged particles with $p_{\perp} \geq 1$ GeV/c, where the particle identification via energy loss measurement provided by the TPC is no longer sufficient to distinguish between pions and electrons [9]. To achieve this, the TRD makes use of transition radiation, which is explained in Section 2.1. Additionally, it is designed to trigger on electrons with high transverse momenta, and on jets. Section 2.2 gives a short overview of the layout, while Section 2.3 explains the working principle of the TRD in greater detail. In Section 2.4, the triggering structure is shortly illustrated. Finally, in Section 2.5, the commissioning for Run 2 is presented.

2.1 Electron identification with transition radiation

A frequently used method to measure the mass of a particle of known momentum, and thus identify it unambiguously, is to measure its specific energy loss $-\frac{dE}{dx}$, as done for example by the TPC. However, for large momenta the mass dependence of the energy loss becomes too small to still provide electron/pion separation. Therefore, the production of transition radiation by electrons in this particular momentum regime can be exploited as an additional measurement for the electron identification.

Transition radiation (TR) is a form of electromagnetic radiation caused by a relativistic charged particle traversing the boundary of two media with different dielectric constants. It is dependent on the Lorentz factor $\gamma = \frac{E}{mc^2}$ of the particle, and only becomes relevant for $\gamma \gtrsim 1000$. Consequently, for a momentum range of a few GeV/c, a lighter particle like an electron will emit TR, while heavier particles (like pions) will not. This transition radiation is detected by the TRD, which in this way complements the PID information of TPC and ITS in addition to providing a trigger on electrons [10].

2.2 Layout of the TRD

The TRD consists of 18 supermodules (SM) installed in the central barrel of ALICE in the space frame, covering the full azimuth and a range in pseudo-rapidity of $-0.9 \leq \eta \leq 0.9$. Each of the supermodules in turn comprises a total of 30 detector modules, so-called read-out chambers (see Section 2.3.1), arranged in five stacks (in z direction) of six layers (in r direction) as illustrated in Figure 2.1.

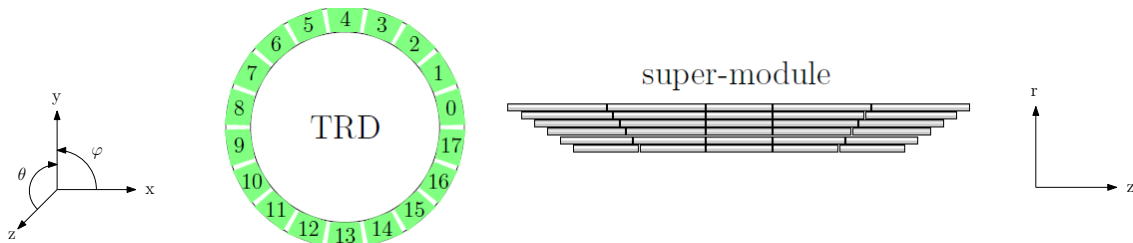


Figure 2.1: Overview of the detector structure: The left side shows a front view of the full TRD, including the numbering of the sectors corresponding to the supermodules. On the right, a side view of one supermodule is shown. (adapted from [8])

In the three supermodules in Sectors 13, 14 and 15, the central stack 2 has been left out to reduce the material budget in front of PHOS. Mounted on each Read-Out Chamber (ROC) is the Front-End Electronics (FEE, see Section 2.3.2), distributed over 6 - 8 Read-Out Boards (ROB). The set-up of the TRD, up to the smallest constituents of the read-out boards, the Multi-Chip Modules (MCM), is shown in detail in Figure 2.2.

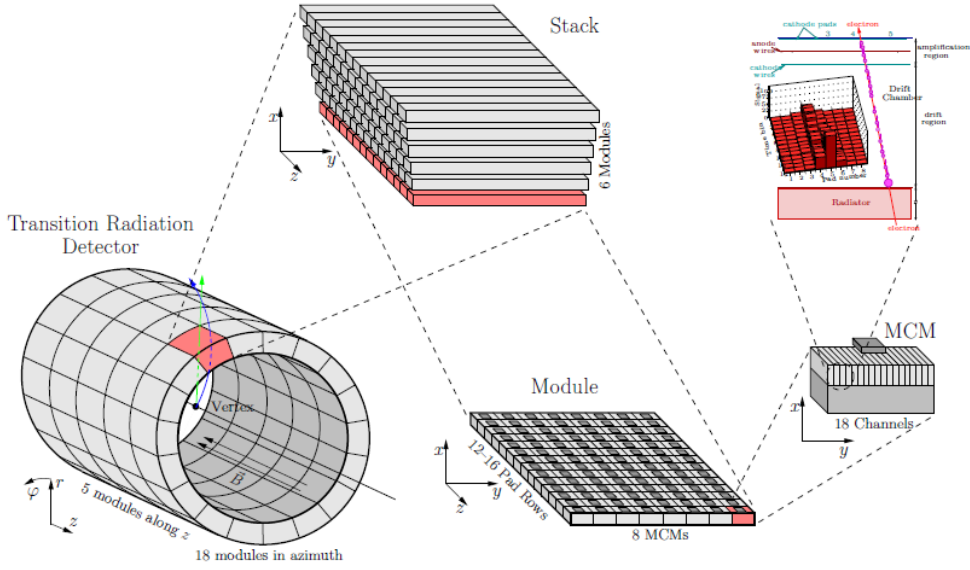


Figure 2.2: Set-up of the TRD: The 18 supermodules each consist of 5 stacks along z direction, which in turn are composed of six layers of drift chambers. A single drift chamber comprises up to 16 rows of read-out pads with 8 MCMs per row, while every MCM provides read-out for 18 pads (see Section 2.3.2 for more information). [11]

2.3 Principle of operation

2.3.1 Read-out chambers

Particle detection and identification in the TRD is based on gas ionisation in the active volume of the read-out chambers. The chambers are composed of a radiator, a drift region filled with a Xe-CO₂ mixture, and a Multi-Wire Proportional Chamber (MWPC) section, made up of a cathode wire plane, an anode wire plane, and a cathode pad plane.

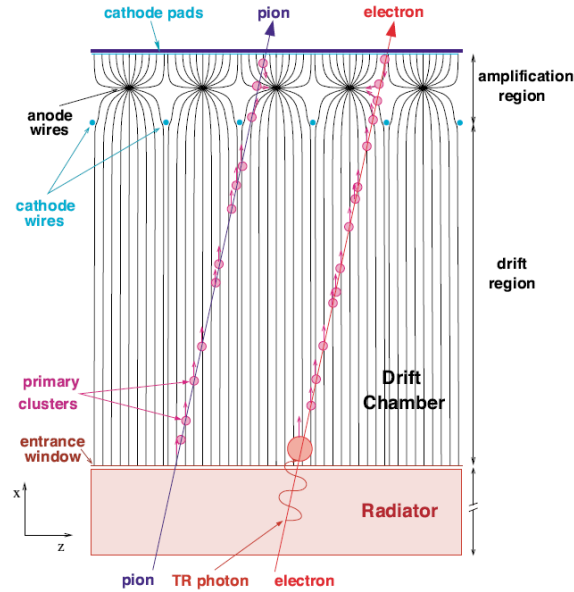


Figure 2.3: Cross-section of a read-out chamber. It consists of a radiator for possible TR production, a drift region with a homogeneous electric field (as indicated by the parallel lines), and an amplification region built as a MWPC. [9]

As illustrated in Figure 2.3, a charged particle traversing a ROC at first crosses the radiator, made up of several layers of foam and fibres with an overall thickness of 48 mm, where it may cause transition radiation (as shown in red for the case of an electron). This choice of radiator material and thickness allows for the TRD to produce ~ 1.45 TR photons per chamber within an energy range of 1 - 30 keV for each electron with a momentum higher than 1 GeV/c [6,8].

Having passed the radiator, the particle ionises the gas mixture in the following drift region before leaving the chamber altogether. In the homogeneous electrical field of the drift region, the electrons originating from the gas ionisation drift towards the cathode wires with a drift velocity of $\sim 1.5 \mu\text{m/s}$. Upon reaching the amplification region between the cathode wires and the cathode pad plane, they are further accelerated, causing avalanches of electrons. The electrons are collected at the anode wires, while the positive ions are slowly drifting back to the cathode wires. The movement of the charges induces a signal on the cathode pad plane which is then further processed by the front-end electronics.

Improvement of Position Resolution

The pad plane of each ROC is divided into 12 - 16 rows in longitudinal direction and 144 columns in azimuthal direction of pads with pad sizes of about 1 cm times 10 cm. The large number of pads in a row and the correspondingly small pad width allows for charge sharing between neighbouring pads, thus improving the resolution in ϕ direction. This is quite important, as the determination of the momentum of the particle depends on the precision of the position measurement.

Since there are considerably fewer pad rows per ROC, the resolution of the z position is limited by the pad length. It is improved by tilting the pads by $\pm 2^\circ$, depending on the layer. Since the pads in layer i are bent in the opposite direction as the pads of layer $i + 1$, combining consecutive layers allows for a more precise determination of the z position of the track.

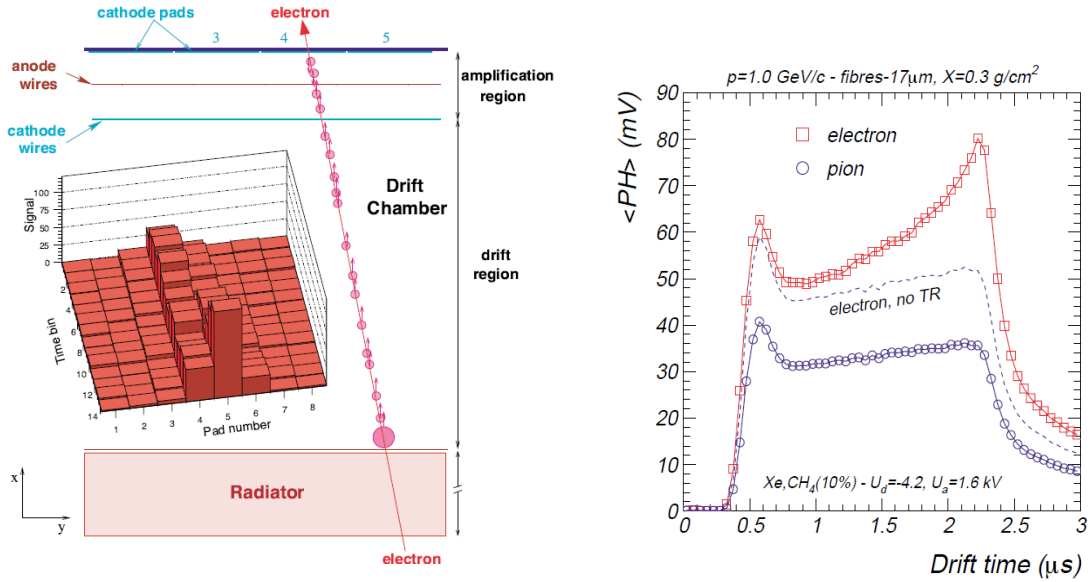


Figure 2.4: Signal formation in the read-out chambers. On the left panel, the signal induced on the pad plane is shown. On the right panel, the average pulse height of the induced signal for both electrons (red squares) and pions (blue circles) is plotted against the drift time. The dashed line additionally illustrates the electron signal without TR. [9]

Signal Generation

An example for the signal induced by an electron is shown in Figure 2.4 on the left. To illustrate the difference between a particle with TR and without TR, the right side of Figure 2.4 shows the average pulse height of the induced signals of an electron and a pion as a function of the drift time. The peak in the beginning shown by both signals is caused by the ionised electrons moving from both sides of the amplification region to the anode wires, while the following plateau corresponds to the electrons from the drift region. If a TR photon is emitted, it will cause a second peak at the end of the drift plateau in later time bins, i.e. close to the chamber entrance. For a pion, on the other hand, the drift plateau stays flat, as it would for an electron with no TR, indicated by the dashed line in Figure 2.4. Due to this TR peak, along with the fact that on average, electrons deposit more energy than pions, an efficient distinction between the two particles is possible.

Particle Identification

Assuming a known drift velocity, the previously described design of the ROCs enables a 3-dimensional reconstruction of the track of the particle needed for the track matching with TPC and ITS. From the curvature of the particle in the longitudinal magnetic field, the transverse momentum can be extracted. Together with the measurement of the energy loss, the mass can be calculated, and thus, as already described in Section 2.1, the particle can be identified.

2.3.2 Front-end electronics

Since the TRD not only provides electron identification via TR, but also serves as a trigger detector (explained in more detail in Section 2.4), the read-out and data processing must occur on a time scale of a few μs [12]. Therefore, the FEE has been installed directly on the read-out chambers and is connected to the pads on the pad plane. The signals from 18 pads are read out and processed by one multi-chip module, so that overall 8 MCMs process the signals of one pad row. To avoid tracking inefficiencies at the boundaries, each MCM is additionally supplied with the signals from one or two pads belonging to the right-sided and left-sided neighbouring MCM, respectively. Depending on the stack, each ROC has a pad plane with 12 - 16 rows, and thus houses a total of 96 - 128 MCMs, distributed over 6 - 8 ROBs. A Detector Control System (DCS) board installed on each chamber, which is accessible via Ethernet connection, is used to control and configure the FEE.

Each MCM is a composition of a Pre-Amplifier/ShAper (PASA) and a TRAcklet Processor (TRAP), which in turn consists of 21 Analog to Digital Converter (ADC) channels, a Tracklet PreProcessor (TPP) and four CPUs. Figure 2.5 shows the signal processing in the MCM: incoming current signals from the pads are pre-amplified by the PASA and then fed into the ADC channels, where they are digitized before being transmitted to the TPP. Subsequently, the TPP filters the data, searches for possible hits, and transfers the information of the selected channels to the CPUs to perform a straight line fit. As this is done for each chamber separately, this fit provides only a part of the entire track through the TRD, a so-called **tracklet**. Besides including the track information from the straight-line fit, each tracklet is assigned a PID value representing the electron likelihood. A more precise description of the tracklet calculation in the TRAP is given in Section 3.2.

2.3.3 On-line tracking

In the TRD, the reconstruction of the track of the particle is split into two parts: At first, the FEE calculates a straight line fit for each possible tracklet, as explained in the previous section. This is called local on-line tracking, as it is executed chamber-wise (further explained in Chapter 3). The tracklets are sent to the Global Tracking Unit (GTU), where in the second stage, also called global on-line tracking, tracks are formed by matching the tracklets within a TRD stack. In the GTU, a linear fit for the entire track is calculated and the track p_{\perp} is extracted, using the offset of the track to the primary vertex [8]. After calculating the PID of the track as the average of the PID values of the contributing tracklets, the track can now be used for the electron and jet triggers.

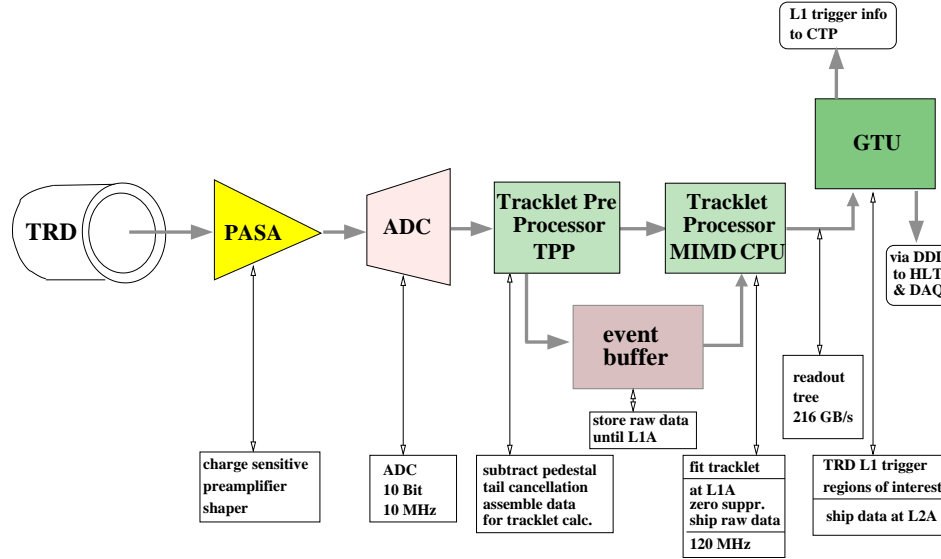


Figure 2.5: Sketch of the signal processing in the FEE [9]. Analog signals coming from the TRD are pre-amplified by the PASA and converted into digital signals by the ADCs. In the TPP the data are filtered and assembled for the calculation of the tracklet fit in the CPUs. The found tracklets are shipped to the Global Tracking Unit (GTU) for further processing.

2.4 Triggering with the TRD

2.4.1 The ALICE trigger system

The amount of data produced in pp and heavy ion collisions is usually so large that a selection of interesting events is needed. For this reason, ALICE uses a three-staged hardware trigger system, with two fast trigger decisions, Level 0 (L0) and Level 1 (L1) after about 1.2 μs and 7.7 μs , respectively, and a slower Level 2 (L2) trigger at about 100 μs after the interaction [10,12]. The global trigger decisions are managed by the Central Trigger Processor (CTP), which receives the trigger inputs at the different time stages, and accordingly distributes the subsequent trigger signals to the detectors. The detectors mainly contributing to the L0 are the forward detectors V0 and T0, as well as central barrel detectors like SPD or EMCal [8]. Detectors that are not fast enough to provide a trigger decision within the low latency of the L0 (for example the TRD), make a contribution to the L1. If the CTP accepts the L1, the TPC is read out, causing the long latency of the L2 of 100 μs , which corresponds to the drift time in the TPC. If the L2 is accepted as well, the data of each detector is transferred to the Data Acquisition (DAQ).

2.4.2 The TRD trigger system

For the TRD, the previously described triggering process must be slightly extended: Since the FEE is in a standby state when not in use, the L0 arrives too late at the TRD to measure the entire signal of a particle passing through. The FEE therefore needs a separate 'wake-up call' to begin read-out. During Run 1, this was achieved using a PreTrigger system (PT) installed in the L3 magnet, which received copies of the T0, V0 and TOF inputs sent in parallel to the TRD (as well as to the CTP) [8]. An overview of the timing for the triggers and data transfer is given in Figure 2.6 After receiving a pre-trigger signal, data acquisition and tracklet calculation begins in the TRAP. If the L0 is issued, the tracklets are shipped to the GTU, where track matching and PID take place. The L1 trigger decision is then sent to the CTP, and, in case of an L1 accept, the buffered raw data is transferred to the GTU to be sent on to the DAQ in case of an L2 accept [13,14].

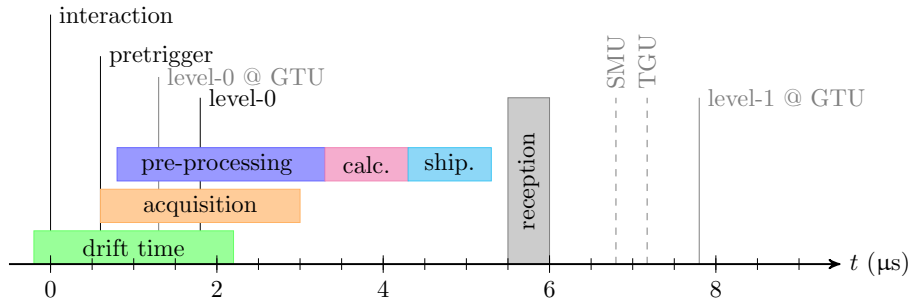


Figure 2.6: Overview of the TRD trigger timing [8]. The wake-up signal generated by the pretrigger starts the data acquisition. After the processing in the TPP and the tracklet calculation, which begin with a small time offset, the tracklets are shipped to the GTU, where they are further processed.

2.5 Commissioning for Run 2

By the end of Run 1 in the beginning of 2013, 13 of the 18 TRD supermodules were installed, as shown in Figure 2.7. During the following Long Shutdown 1 (LS1) in 2013/14, the remaining SMs were transported from their construction site in Münster to CERN for testing and installation. The last SM to be taken to the experimental cavern was Sector 17, because the previously inserted SM had to be exchanged. By the end of November 2014, the installation of the TRD was complete.

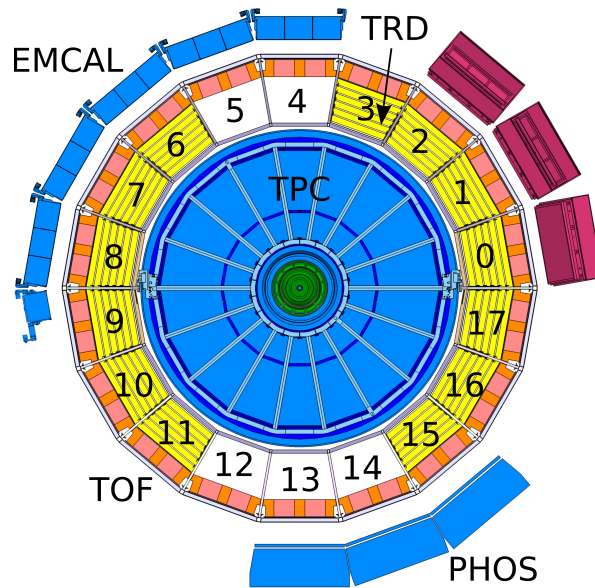


Figure 2.7: Installation status of the TRD by the end of Run 1 in early 2013 [8]. The installation of the remaining 5 supermodules, plus the exchange of the supermodule in Sector 17, were performed during the first long shutdown of the LHC in 2014.

Over the course of this Bachelor thesis, I had the opportunity to participate in the commissioning of the TRD for Run 2. Over the time from September 2014 to January 2015, I made several trips to CERN to assist in the testing of the supermodules that had yet to be inserted, and later in the preparations leading to the first full read-out of the TRD.

Prior to being transported to the cavern, the new supermodules were set up in the clean room on the ALICE site, where they were tested and prepared for their installation. I participated in the testing of the SMs for sectors 4 and 5. This included connecting the SMs to the test set-up in the clean room, specifically the low voltage connections and the optical read-out fibres as well as the Ethernet cables for the DCS boards. I also had a part in testing them, e.g. by measuring the voltage of the low voltage

connections on the SM.

After all supermodules had been inserted and the doors of the magnet had been closed, access to the supermodules was only possible by partaking in both the Self-Rescue Mask and the Confined Space - ALICE training. The successful completion of the trainings allowed me to be of further assistance, especially when the TRD had to be prepared for full read-out for the first calibration runs in 2015. The main tasks in which I took part concerned the testing and, if necessary, repair of the low voltage power supplies and the Ethernet connections of the DCS boards. A number of the low voltage supplies powering the FEE showed faulty behaviour and needed either to be fixed, or entirely replaced. As before in the clean room, I measured the voltage of the power supplies to give further information about possible faults, and exchanged a power supply when necessary. Another problem presented itself when some of the DCS boards on the read-out chambers could not be reached. By swapping the Ethernet cables and re-checking the connections, we were able to find and replace broken Ethernet cables, thus restoring the connection for some of the DCS boards.

Once we had established a condition stable enough to start read-out test, the opportunity arose for me to operate the low voltage and DCS boards from the control room, and to initiate the test runs for the read-out.

3 Local on-line tracking in the TRD

The local on-line tracking provides a parametrisation of the track segments in each read-out chamber (see Section 2.3.3). These tracklets are later matched within the respective TRD stack to form tracks which contain the information on the transverse momentum p_{\perp} of the track and the particle identification.

This chapter describes the procedure of the local on-line tracking. After a short overview of the local coordinate system in Section 3.1, the process of digitizing and filtering the data is discussed in Section 3.2.1. In the next step, the actual calculation of the parameters describing the tracklet is explained (Section 3.2.2) and afterwards, some corrections of systematic errors are shown (Section 3.2.3). At last, a short description of the simulation of the local tracking is given (Section 3.3).

3.1 Local coordinate system

To simplify the description of the local on-line tracking, it is useful to switch from the ALICE global coordinate system [15] to the local coordinate system of the TRD, which is a right-handed Cartesian system, shown in Figure 3.1.

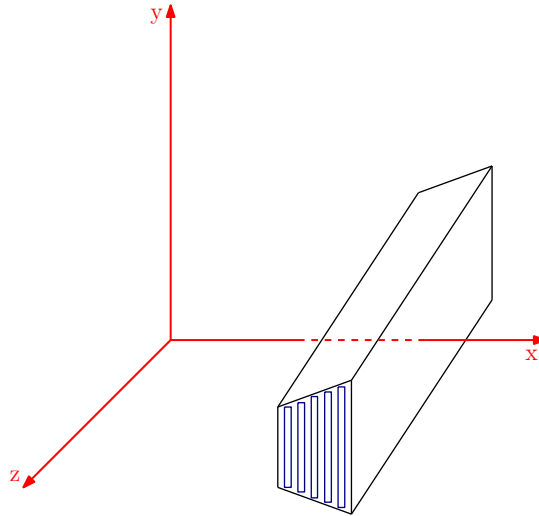


Figure 3.1: Sketch of the local coordinate system for the TRD modules. The x axis points from the origin outwards, intersecting the supermodule in the middle. The y axis points from the chamber centre upwards. The z axis is the same as in the global coordinate system of ALICE.

As in the global coordinate system, the origin of the local coordinate system $(0,0,0)$ is located at the nominal interaction point (IP) of the beams and the z axis coincides with the beam axis, with positive z going in the direction of the anti-clockwise beam (away from the muon arm). The z axis covers a range from $-350 \text{ cm} \leq z \leq 350 \text{ cm}$. The local x axis points outward from the origin and intersects the module in the middle, ranging from about $290 \text{ cm} \leq x \leq 370 \text{ cm}$. The local y axis then specifies the distance from the chamber centre, covering a minimal range of $-47.8 \text{ cm} \leq y \leq 47.8 \text{ cm}$ (for the bottommost layer) and a maximal range of $-58.9 \text{ cm} \leq y \leq 58.9 \text{ cm}$ (for the topmost layer) [9, 13].

3.2 Tracklet calculation and tracking procedure

3.2.1 Signal filtering and digitization

In the first step, the signals from the pad plane are transferred to the MCMs on the FEE (see Section 2.3.2) where they are digitized by the ADCs in the TRAP and sampled in timebins of 100 ns. Afterwards, the digital data pass through a configurable filter chain, consisting of a non-linearity filter, a pedestal filter, a gain filter, a tail cancellation filter, and a cross talk filter. Of these five, only the

pedestal filter and the gain filter were used during Run 1, as they are important for the channel-by-channel correction of offsets and non-uniform gains, respectively. The purpose of the tail cancellation filter is to subtract the signal caused by the slow ion tails of the input signal, and in that way improve the angular resolution of the tracklets. However, at the same time the tail cancellation worsens the signal-to-noise ratio, and thus the online PID calculations. Therefore, it was only used for test runs so far [8].

3.2.2 Tracklet calculation in the TRAP

After the data have been digitized and filtered, they are sent to the TPP, which searches for clusters in each timebin. For the TPP to accept the signal, the charge Q_i of the cluster in a channel i must be a local maximum with respect to the two neighbouring channels, and the sum of the three channels must exceed a given threshold:

$$Q_i \geq Q_{i-1} \quad \text{and} \quad Q_i > Q_{i+1},$$

$$Q_{i-1} + Q_i + Q_{i+1} \geq Q_{thr}.$$

For up to four detected clusters the y position is calculated as the centre of gravity from the charge of the three adjacent channels. In preparation of the straight line fit which describes the tracklet the following fit sums are computed in the preprocessor for each channel i and timebin t [8]:

$$N_i = \sum_{t=t_{fs}}^{t_{fe}} \mathbb{1}_i(t), \quad X_i = \sum_{t=t_{fs}}^{t_{fe}} \mathbb{1}_i(t) \cdot t, \quad X_i^2 = \sum_{t=t_{fs}}^{t_{fe}} \mathbb{1}_i(t) \cdot t^2,$$

$$Y_i = \sum_{t=t_{fs}}^{t_{fe}} \mathbb{1}_i(t) \cdot y_i(t), \quad XY_i = \sum_{t=t_{fs}}^{t_{fe}} \mathbb{1}_i(t) \cdot t \cdot y_i(t),$$

$$Q_{0,i} = \sum_{t=t_{qs0}}^{t_{qe0}} \mathbb{1}_i(t) \cdot Q_i, \quad Q_{1,i} = \sum_{t=t_{qs1}}^{t_{qe1}} \mathbb{1}_i(t) \cdot Q_i.$$

In these equations, $\mathbb{1}_i(t)$ indicates that a cluster has been found, and t_{fs} and t_{fe} mark the beginning and end of the time measurement used for the linear fit.

If the two conditions

$$N_i \geq N_{CL}^{thr}, \quad N_i + N_{i+1} \geq N_{CT}^{thr},$$

where N_{CL}^{thr} and N_{CT}^{thr} are configurable values in the TRAP, are fulfilled by clusters on two neighbouring pads i and $i + 1$, the preprocessor accepts them as a possible tracklet candidate and forwards the data to one of the CPUs in the TRAP. In this way, up to four tracklet candidates are chosen and sent to the four CPUs; if there are more than four channels with a possible tracklet, those with the highest number of hits are selected.

In the CPUs, the calculation of the linear fit takes place. As a first step, the fit sums of the clusters from the two adjacent channels i and $i + 1$ are merged:

$$N = N_i + N_{i+1}, \quad X = X_i + X_{i+1}, \quad X^2 = X_i^2 + X_{i+1}^2,$$

$$Y = Y_i + Y_{i+1} + w_{pad} \cdot N_{i+1}, \quad XY = XY_i + XY_{i+1} + w_{pad} \cdot X_{i+1},$$

$$Q_0 = Q_{0,i} + Q_{0,i+1}, \quad Q_1 = Q_{1,i} + Q_{1,i+1}.$$

The additional terms in the calculations for Y and XY account for the shift of one pad width w_{pad} for channel $i + 1$.

In order to parametrise the straight-line fit as

$$y(t) = y + b \cdot t,$$

the CPUs now proceed with the merged fit sums to calculate

$$y = \frac{X^2 \cdot Y - X \cdot (XY)}{N \cdot X^2 - X \cdot X}, \quad b = \frac{N \cdot (XY) - X \cdot Y}{N \cdot X^2 - X \cdot X},$$

where y is the transverse position (in units of a pad width) relative to the chamber centre and b is the slope (in units of pads per timebin). However, instead of using the slope to describe the tracklet, the deflection d_y over the drift length l_{drift} is calculated:

$$d_y = b \cdot w_{pad} \cdot n_{drift}, \quad n_{drift} = \frac{l_{drift}}{v_{drift}}.$$

The transverse offset is given at the radial position corresponding to timebin 0, which is at a slightly larger radius than the anode wire plane (see Figure 3.2). To translate this position into a global coordinate, a channel-specific offset is added, and the sum is then scaled by the pad width. The tracklet parametrization with transverse position y and deflection d_y is shown in Figure 3.2. Together with the longitudinal position z obtained from the pad row of the MCM, and a PID value from a look-up table based on the charge sums Q_0 and Q_1 , they form the parameters for the full tracklet description.

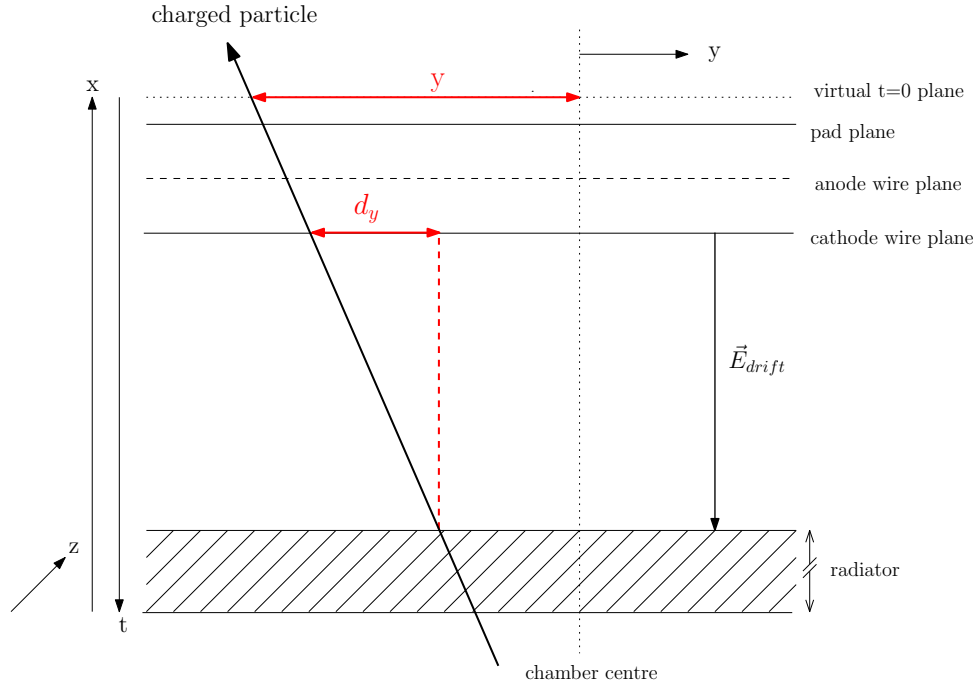


Figure 3.2: Illustration of the straight line fit performed in the local on-line tracking: The tracklet is parametrised by the transverse position y relative to the chamber centre and the deflection d_y over the drift length of 3 cm. y is measured at the radial position corresponding to timebin 0. (figure adapted from [8])

3.2.3 Position and deflection corrections

Before the parameters from the linear fit can be further used, several cuts and corrections have to be applied in the MCMs:

Pad tilting: The tilting of the pads on the pad plane results in a correlation of the y and z position [9], which also affects the deflection of all tracks that leave the chamber at a different z position than the one at which they entered.

The correction of the transverse position cannot be done on MCM level, because the MCMs cannot determine the z position with more precision than one pad length. For the deflection however, the knowledge of the pad row is precise enough to correct the influence of the tilted pads directly on the MCMs by assuming that the particle track points to the primary vertex.

Lorentz deflection: Due to the longitudinal magnetic field of $|B| = 0.5$ T generated by the L3 magnet housing the central barrel, particles traversing ALICE are bent depending on their charge and the direction of \vec{B} . Since the momentum of the primary particles is large enough for the curvature to be neglected over the length of the chamber, the straight line fit used in the local on-line tracking is still valid. However, as illustrated in Figure 3.3, the electrons originating from the ionisation of the gas in the drift region are much slower and therefore affected by the Lorentz drift. This causes an additional offset $d_{y,L}$ to the deflection which has to be corrected during the deflection calculation in the MCMs. The correction can be derived using the Lorentz angle Ψ_L , given by $\tan \Psi_L = \omega\tau$, as

$$d_{y,L} = -l_{drift} \cdot \omega\tau \cdot \text{sgn}(B),$$

with ω being the cyclotron frequency and τ the mean time interval between two collisions of electrons and gas [14]. Figure 3.4 illustrates the Lorentz correction in the MCMs by comparing the uncorrected deflection of the tracklets (Figure 3.4a) with the corrected deflection (Figure 3.4b), which ranges roughly from -0.8 cm to 0.8 cm. In this case a positive magnetic field of 0.5 T was used, resulting in a positive Lorentz correction of ~ 0.5 cm.

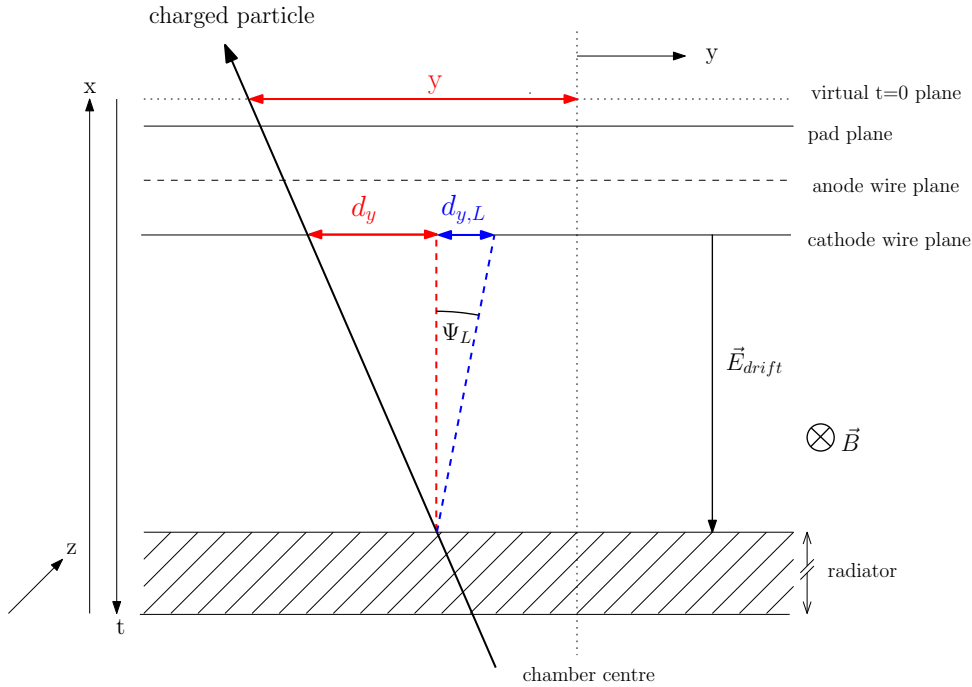


Figure 3.3: Lorentz correction: Under the influence of a magnetic field, the electrons from the primary ionisation are diverted from their path, causing an additional offset to the deflection which has to be corrected. (figure adapted from [8])

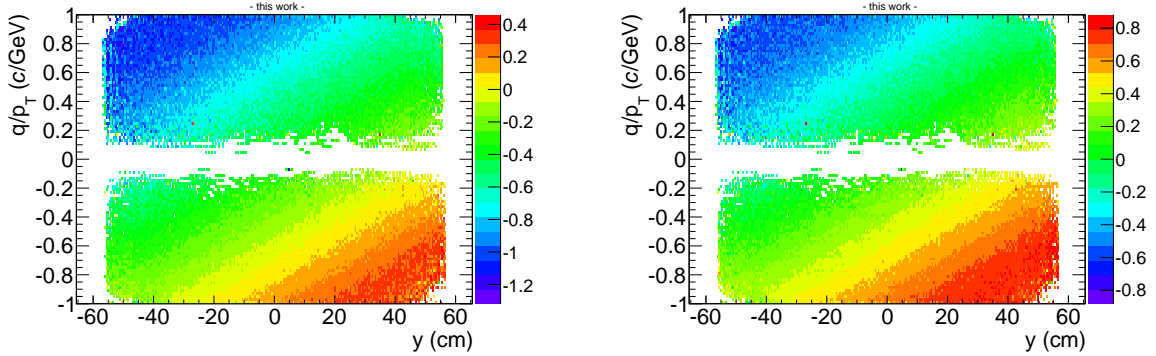
Deflection range: For the trigger decision, a first p_T cut can be used to reduce the number of tracklets. This in turn results in a restriction to the deflection length, which is position-dependent [8, 13]:

$$d_{\pm} = l_{drift} \cdot \tan \left(\varphi \pm \arcsin \left(\frac{R}{2} \cdot \frac{0.3 \cdot B/T}{p_T^{min}/(GeV/c)} \right) \right), \quad \varphi = \arctan \left(\frac{y}{x} \right).$$

The maximum range of the deflection $-8.8 \text{ mm} \leq d_y \leq 8.8 \text{ mm}$ [11] leads to a position-dependent lower bound of the transverse momentum. However, this is outside the p_{\perp} range of interest for the TRD trigger, as shown in Figure 3.4b.

If a tracklet passes these cuts, the corrected values of y , d_y , z and the PID are written to the so-called tracklet word, which is then shipped to the GTU to be matched with other tracklets, resulting

in the final track of the particle in the TRD.



(a) Deflection correction undone. The deflection ranges roughly from -1.2 to 0.4 cm.

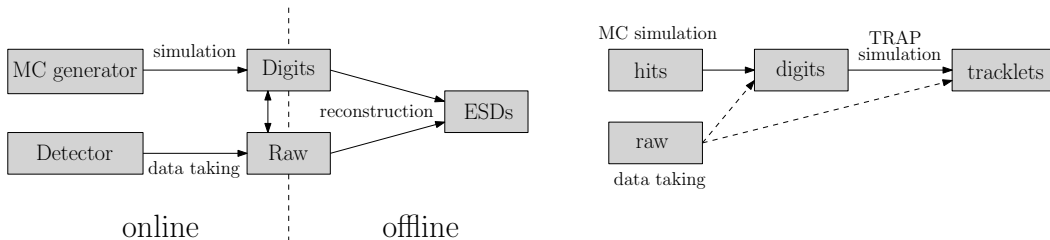
(b) Deflection with correction applied. Note the change in the colour scale: The deflection now ranges roughly from -0.8 to 0.8 cm.

Figure 3.4: The tracklet deflection (in cm) over the drift length of 3 cm is shown depending on the y position and q/p_{\perp} .

3.3 Tracklet simulation

In general, the ROOT-based AliRoot framework [16] is used to process both raw data read out from the detector and data generated in a Monte Carlo (MC) simulation. The raw data can either be directly reconstructed, or translated to digits, which can also be obtained from a MC simulation of the detector, as illustrated in Figure 3.5a. The output of the reconstruction are Event Summary Data (ESD) written to `AliESDs.root` files, which can then be used for further analyses.

In Figure 3.5b, the simulation and reconstruction chain is shown for the more specific case of the local on-line tracking: Again, the raw data from the detector as well as hits from MC simulations are available as digits, which contain the ADC data and can be used to simulate tracklets (and ultimately tracks for the global tracking). Tracklets can also be directly extracted from the raw data, which allows for a direct comparison between raw and MC data, or original and re-simulated raw data, for instance. This also motivates the use of MC simulations to study the influence of different configuration settings and algorithms, which allows for an easy comparison of MC truth to the simulated tracklets (explained in more detail in the following chapter). The simulation of the local on-line tracking in the TRAP, as described in Section 3.2, is implemented in the `AliTRDmcmSim` class, while the tracklets are made available in the `AliESDTrdTracklet` class. For the simulation to be able to produce results as close to the hardware as possible, the different configurations of the TRAP used during the runs are stored in the Off-line Condition DataBase (OCDB) as objects of the `AliTRDtrapConfig` class.



(a) Tracking simulation and reconstruction: Data originating either from Monte Carlo simulations or from data taking in the detector are reconstructed and the results stored in the ESDs.

(b) Local on-line tracking simulation: Based on the digits provided by raw or simulated data, tracklets are simulated by the TRAP. Alternatively, the tracklets can originate directly from the raw data.

Figure 3.5: Overview of the tracking simulation (adapted from [8])

4 Optimisation of the local on-line tracking

The local on-line tracking plays an important part in the trigger scheme of the TRD, as the tracklets provide the information about position, deflection and PID. Therefore, optimising the local on-line tracking is desired in order to improve the trigger performance.

In this thesis, the optimisation of the local on-line tracking is performed using Monte Carlo simulations. As described in Section 3.3, Monte Carlo simulations can be used to reproduce the results the real detector, allowing to easily compare the found tracklets to the Monte Carlo truth. From this comparison, tracklet efficiencies or shift distributions can be extracted to judge the tracklet quality, and the effect of different TRAP settings and algorithms on the performance can be studied. The general approach is explained in Section 4.1. The following sections illustrate the steps to improve the local on-line tracking. Section 4.2 focuses on tracklets that are found more than once per "true", i.e. Monte Carlo, particle. Since these multiple tracklets deteriorate the PID performance, they need to be sorted and rejected, so that only the one with the full charge is left. Both the deflection d_y and the transverse position y are subject to corrections, which are realised in Sections 4.3 and 4.4. As a last point, the mis-alignment of the individual chambers relative to each other is taken into account and corrected in Section 4.5.

4.1 General procedure

The Monte Carlo simulations used in the following sections are minimum bias pp collisions at $\sqrt{s} = 8$ TeV, produced specifically for this thesis. For Sections 4.2 to 4.4 an ideal Monte Carlo simulation without gain variations or mis-alignment was used. In Section 4.5, which targets the chamber-wise mis-alignment, a Monte Carlo simulation which takes into account the mis-alignment was used instead.

To extract the tracklet information from the ESDs and compare them to the Monte Carlo truth, an off-line analysis task¹ was implemented. As a first step, Monte Carlo track references, which are defined as the first and last point where a particle deposits energy in the active volume of a TRD chamber during the detector simulation, are extracted from the Monte Carlo events. To reduce the number of such track references, several cuts are applied to select only those that are relevant for the local on-line tracking. Since only primary charged particles with a transverse momentum higher than 1 GeV/ c are of interest for the triggering, a corresponding p_{\perp} cut as well as cuts on tracks from the primary vertex and on the charge are included. Additionally, only tracks from electrons and pions are taken into account. Lastly, if the track reference is not found in the local x range of the TRD (see Section 3.1), it is discarded. Having passed these cuts, the track references are matched into pairs by applying cuts both on their difference in x , and their deflection over the drift length. If these cuts are passed as well, the pair of track references is defined as a "findable" tracklet and can be compared to tracklets that are actually found by the detector.

As a next step, for each pair of track references the tracklets are extracted from the ESD events and matched using the Monte Carlo labels and checking for spatial proximity. This is the starting point for the comparison of the Monte Carlo truth, i.e. the track references, with the simulated detector response, i.e. the tracklets.

4.2 Tracklet selection

As a first step to improve the local on-line tracking, the correction of finding multiple tracklets per track reference pair is targeted. To illustrate the situation, the number of tracklets per track reference pair is counted depending on q/p_{\perp} , as shown in Figure 4.1.

The occurrence of more than one found tracklet per expected one can be explained by the requirement of the local tracking algorithm for two neighbouring channels to exceed a certain charge threshold, as outlined in Section 3.2. If the clusters are spread over more than one pad, it is possible that a tracklet candidate in channel i (with $N_i + N_{i+1} \geq N_{CT}^{thr}$) is found, and that the rest of the signal is mistaken for a second tracklet candidate in channel $i + 1$ (with $N_{i+1} + N_{i+2} \geq N_{CT}^{thr}$). If this is the case, the tracklet found in channel i is attributed the original charge of the particle, but the tracklet found in channel $i + 1$ only has a fraction of the original charge, thus deteriorating the PID.

¹The analysis task is a C++ class integrated in the analysis framework of ALICE, which provides tools for efficient data processing [16].

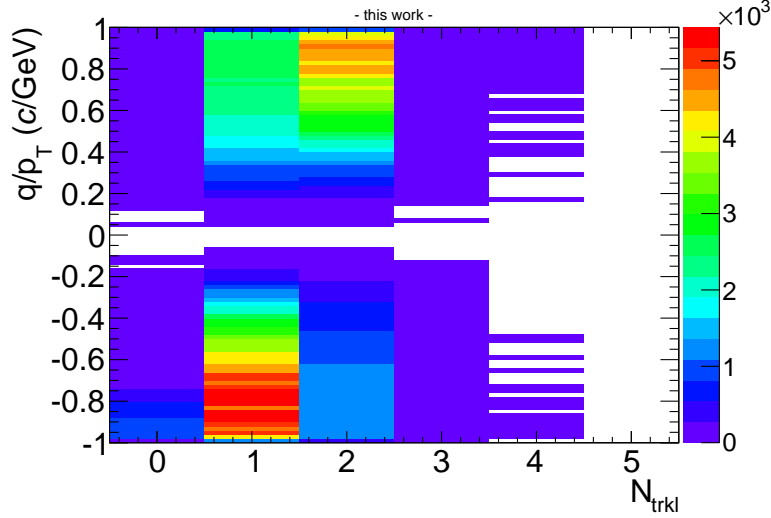


Figure 4.1: Number of findable tracklets per track reference pair: Tracklets are found more than once per pair of Monte Carlo track references, especially for positively charged particles.

The appearance of multiple tracklets is especially distinctive for positively charged particles, which are most probably found twice per track reference pair (see Figure 4.1). For positive tracklets, being bent in the direction opposite to the Lorentz drift, the apparent inclination angle is larger and the clusters are spread over more pads on average (illustrated in Figure 4.2).

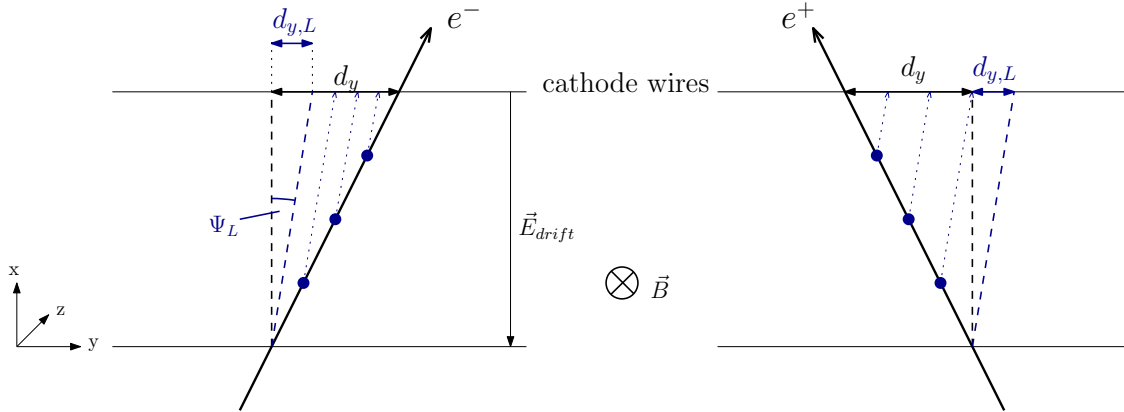


Figure 4.2: Positively charged particles are spread over more neighbouring pads, resulting in tracklets being found twice or more although belonging to the same particle (in this case given by a pair of track references)

A possibility to improve the PID is to keep only the tracklet with the highest charge and discard the others. This was first tested in the off-line analysis task by implementing an algorithm to select the tracklet with the full charge. The matching of the tracklets to the track references (described in the previous section) was used to find all tracklets belonging to one pair of track references. In the selection algorithm, the PID values of up to four tracklets found more than once per track reference were compared. The maximum of four tracklets per track reference was chosen based on Figure 4.1. Since a linear look-up table for the PID values was used, the highest PID value corresponds to the highest charge, and thus allows for the selection of the "best" tracklet.

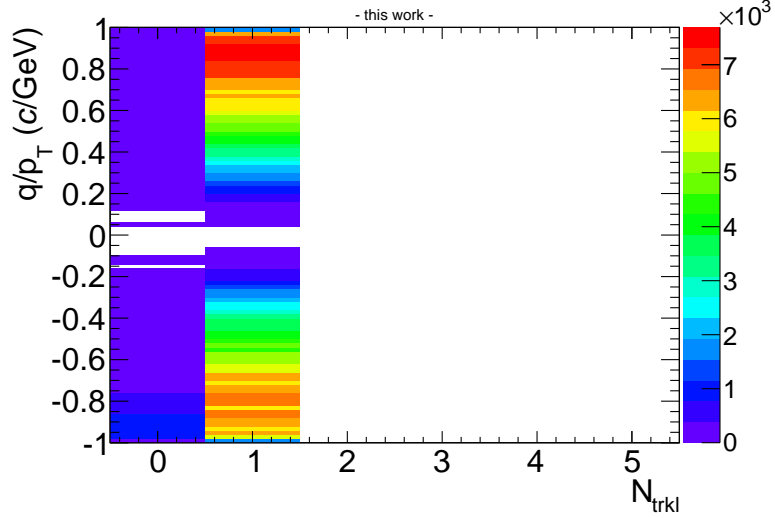


Figure 4.3: Number of tracklets per pair of track references after the tracklet selection was performed in the off-line analysis task. For all tracklets that were found more than once, only the one with the highest charge is kept, the others are discarded.

The implementation in the analysis task provides the best possible result, as shown in Figure 4.3, and was therefore employed in the following steps to improve the on-line tracking, as described in the next paragraphs.

However, it is not possible to apply the tracklet selection in this way on the MCMs to be used for actual data taking, since each MCM is limited to processing the data of its own channels, and has no notion of tracklets being found in neighbouring MCMs. Therefore, the tracklet selection can only be performed on each MCM individually by comparing neighbouring channels and choosing the tracklet candidate with the highest charge sum while rejecting the rest. To test the effectiveness of such a tracklet selection, a corresponding algorithm was implemented in the `AliTRDmcmSim` class. The result is shown in Figure 4.4:

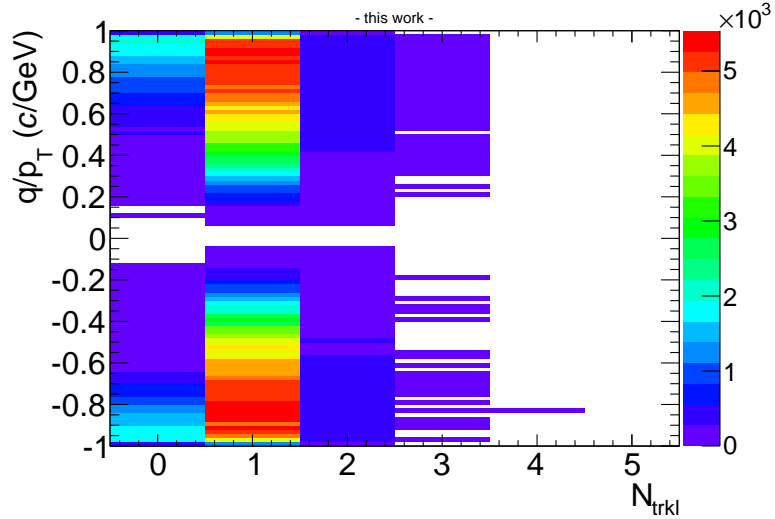


Figure 4.4: Number of tracklets per pair of track references after the tracklet selection on the MCMs. The larger part of the multiple tracklets has been removed, but some tracklets are still found more than once.

The tracklet selection clearly decreases the occurrence of multiple tracklets, as the most probable number of tracklets per track reference pair is now one independent of the charge. Still, some tracklets

are found more than once, but now the number of multiple tracklets is reduced to $\sim 7\%$, compared to $\sim 40\%$ before the selection (see Figure 4.1).

The remaining multiple tracklets belong to tracklets on the borders of two neighbouring MCMs. To illustrate this, Figure 4.5 shows the y and z positions of all tracklets that are found more than once, for Layer 0 in Figure 4.5a and Layer 5 in Figure 4.5b.

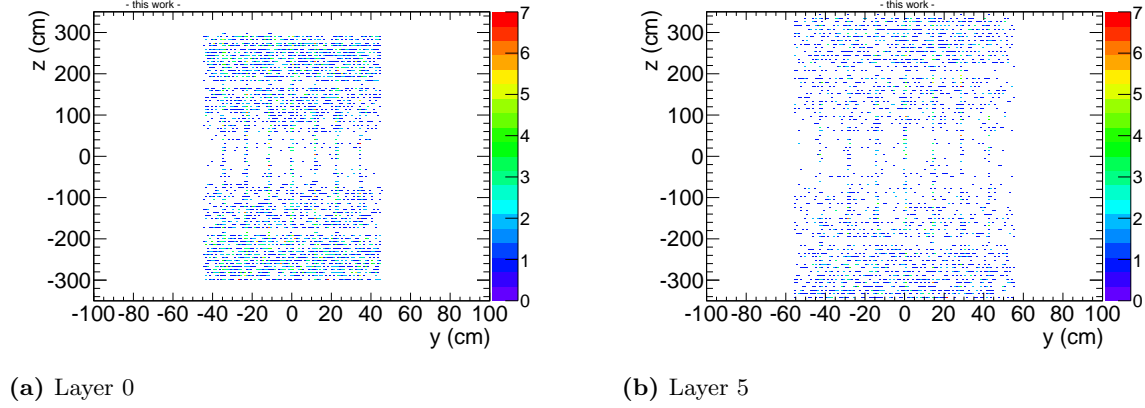


Figure 4.5: Position of multiple tracklets, shown for Layers 0 and 5. The efficiency of the tracklet selection decreases for increasing $|z|$ due to tracklets being spread over more than one pad row.

For small $|z|$, the structure of the MCM borders is visible as horizontal lines. As every MCM processes the signal from 18 pads, the difference in y between the lines corresponds roughly to 18 times the pad width, which is 0.65 cm for Layer 0 and 0.80 cm for Layer 5 [9]. However, for increasing values of $|z|$ the efficiency of the tracklet selection decreases. This suggests that the multiple tracklets are spread not only over adjacent pads in one row (i.e. in y direction) but also over pads in one column (i.e. in z direction). For large values of $|z|$, the tracklets are bent further in z direction, increasing the probability of the charge to spread over two neighbouring pad rows, while for small z , the tracklets are hardly bent in z direction and the charge is most likely read out on the pads in only one pad row. The charge sharing in z direction cannot be fixed in the local on-line tracking. Still, it can be verified by implementing another tracklet selection in the off-line analysis task. Now only multiple tracklets belonging to the same z row are chosen and their position plotted, as shown in Figure 4.6. The borders of the MCMs are now clearly visible independent of the z position.

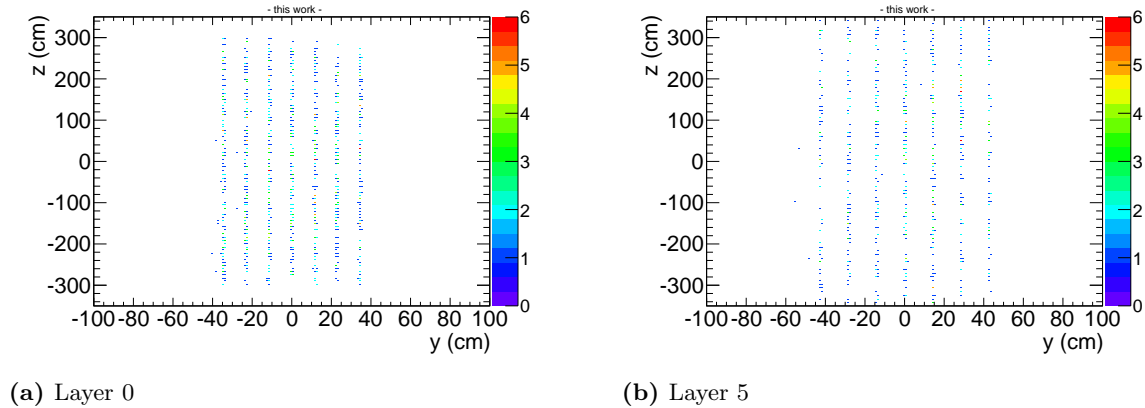
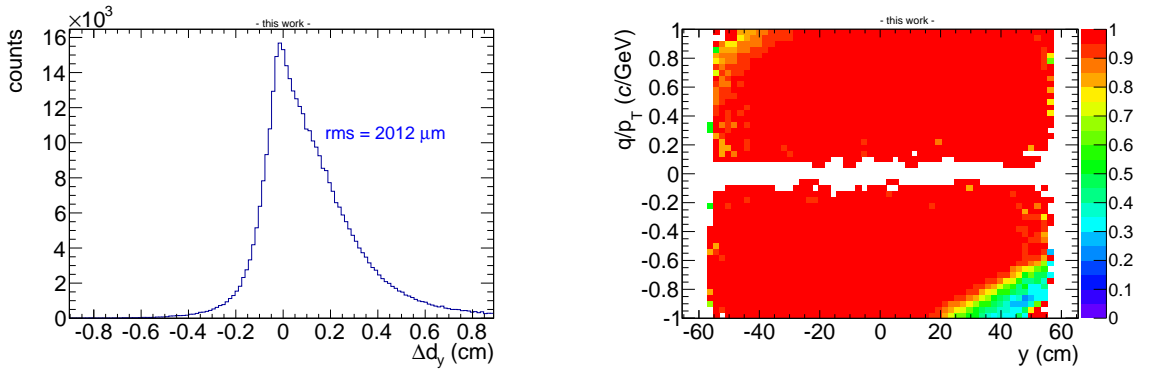


Figure 4.6: Position of multiple tracklets, shown for Layers 0 and 5, now only with multiple tracklets from the same z row. The borders of the neighbouring MCMs are clearly visible.

4.3 Drift velocity

The next step to improve the on-line tracking is to optimise the calculation of the straight line fit describing the tracklet. In this section, we take a closer look at the deflection d_y , while in the next section, the transverse position y is studied in detail.

To judge the quality of the tracklets, the tracklet deflection is compared to the deflection of the track references, which is scaled to the drift length of 3 cm. This can be done by studying the distribution of the deflection shift Δd_y , which is calculated as $\Delta d_y = d_{y,sim} - d_{y,MC}$. In this equation, "sim" represents the tracklets, while "MC" identifies the track references. The resulting distribution, shown in Figure 4.7a, is quite broad and rather asymmetric. This asymmetry is visible also in the tracklet efficiency, see Figure 4.7b, which is determined as the fraction of track reference pairs with at least one found tracklet. It is close to unity except for negative q/p_\perp and large y , because the deflection of these tracklets is too large to pass the cut of the accepted deflection range. The same effect should be seen for positive q/p_\perp on the other side of the chamber, but it is hardly visible.



(a) Distribution of the deflection shift
 $\Delta d_y = d_{y,sim} - d_{y,MC}$

(b) Tracklet efficiency depending on the y position

Figure 4.7: Plots for to illustrate the deficiencies of the deflection d_y

The explanation for the asymmetries in both plots is given by the ion tails of the signals: Since the movement of the positive ions in the amplification region is slow, the signal is induced not only in one timebin, but in the following timebins on the same pad as well. This results in a superposition of the signals in consecutive timebins, as illustrated in Figure 4.8.

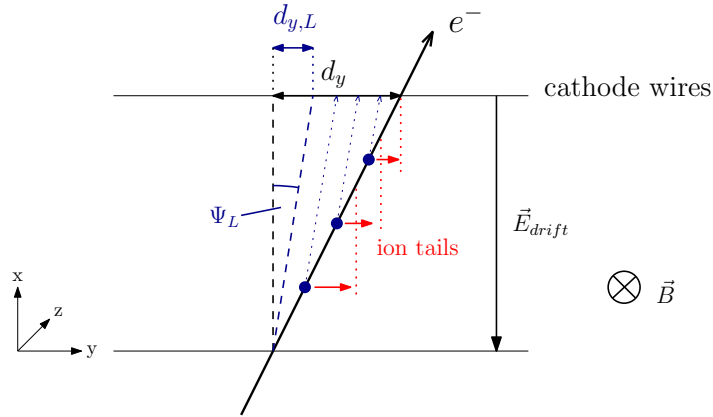


Figure 4.8: The slow movement of the positive ions results in an overlap of the signal on one pad in consecutive timebins, as indicated by the red dots.

This in turn affects the tracklet deflection as shown in Figure 4.9: In black, the track of the Monte Carlo particle through the chamber is illustrated, meaning that the deflection d_y corresponds to the "true" deflection $d_{y,MC}$. The blue line represents the tracklet with only the magnetic field (and no ion tails), with $d_{y,L}$ being the Lorentz correction (as in previous figures). Finally, the tracklet as measured in the detector is shown in red, with d'_y being the measured deflection. If the Lorentz correction is now applied to d'_y , we arrive at the tracklet deflection $d_{y,sim}$, as introduced before. As indicated in Figure 4.9, $|d_{y,sim}|$ is shifted to smaller values compared to $|d_{y,MC}|$, which results in the broad width of the Δd_y distribution. This effect is stronger for positively charged particles, since the signal is spread over more pads. The asymmetry of the Δd_y distribution can be explained by this as well as the efficiency, since the deflection of the positive tracklets is shifted to values small enough to pass the deflection cut even at the far end of the chamber after the Lorentz correction has been applied.

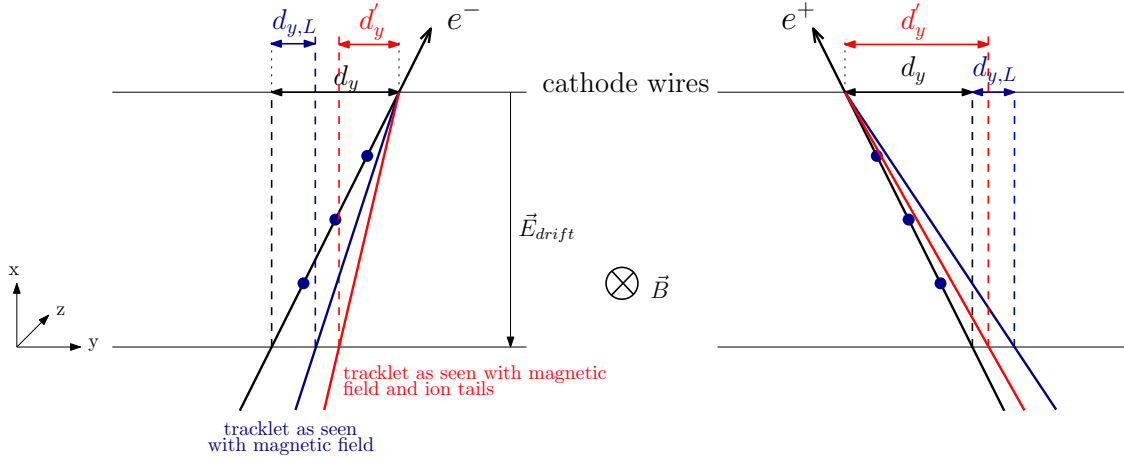
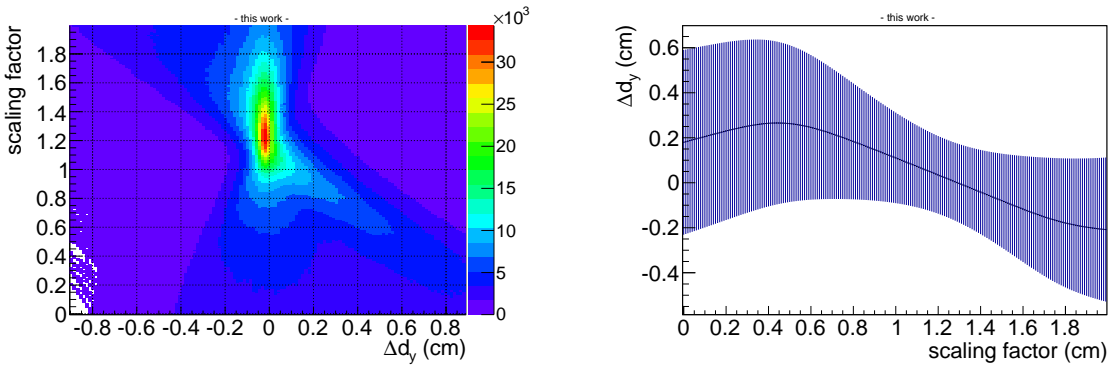


Figure 4.9: The reconstructed deflection $d_{y,sim} = d'_y + d_{y,L}$ is shifted to smaller absolute values due to the effect of the ion tails.

To compensate the effect of the ion tails and revert the deflection to its original value, we can make use of the configured drift velocity by understanding it as an effective quantity that can be set in the TRAP configuration. As d_y is dependent on v_{drift} (see Section 3.2.2), finding the right value for v_{drift} will minimize the deflection shift Δd_y .



(a) The deflection shift Δd_y is shown depending on the scaling factor.

(b) Profile obtained from the left plot. The spread around the average value of Δd_y is smallest for a scaling factor around ~ 1.2 .

Figure 4.10: Determination of the scaling factor

In the `AliTRDtrapConfig` class, instead of the drift velocity the number of timebins corresponding to the drift length is configured with a precision of 2^{-5} . Tuning the drift velocity therefore translates to tuning the number of timebins, which was set in the previous simulations as $n_{drift} = 620/32$ timebins = 19.375 timebins. We can now define a scaling factor in a range from 0 to 2 to vary n_{drift} until we find the optimal value, for which the width of the shift distribution is minimized. To avoid running a new simulation for each new scaling factor, the tuning is done in the off-line analysis task instead. In Figure 4.10a the deflection shift depending on the scaling factor is plotted, and a profile obtained from this plot is shown in Figure 4.10b. The width of the distribution around the average in Figure 4.10b is smallest for a value of ~ 1.2 , which sets a range of interest for the determination of the scaling factor. For each scaling factor within this (arbitrary) range, a Δd_y distribution and the corresponding rms value are obtained from the plot in Figure 4.10a. In the next step, the rms values are plotted as a function of the scaling factor and a second degree polynomial is used to extract the correct value from the minimum (see Figure 4.11).

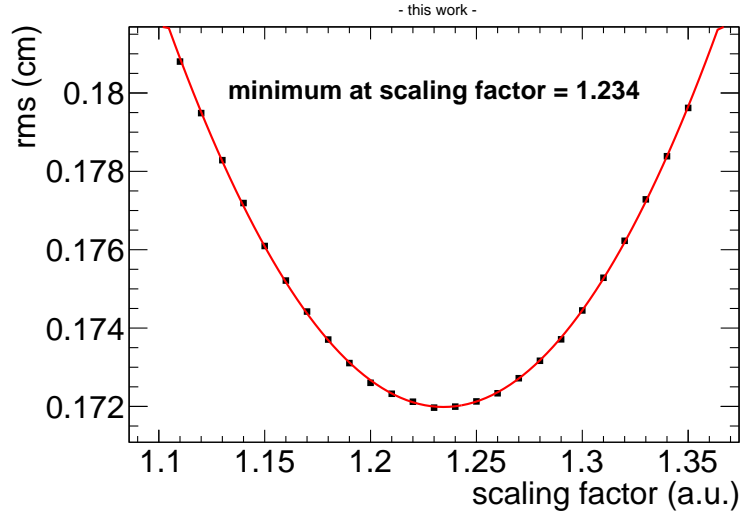
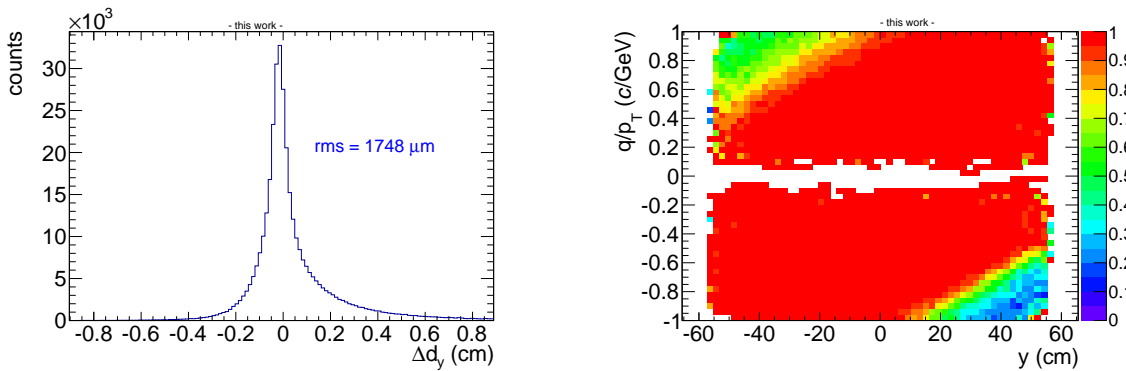


Figure 4.11: A second degree polynomial is used to fit the distribution of the rms values. From the minimum, the optimal scaling factor is obtained.



(a) Distribution of Δd_y after the setting of the new value for n_{drift} . Both width and symmetry have been improved.

(b) Tracklet efficiency depending on the y position after the setting of the new value for n_{drift} . The distribution is more symmetric, resulting in an additional loss of positive tracklets at small y .

Figure 4.12: Results of the drift velocity correction

The determined scaling factor of ~ 1.234 considered with respect to the originally set value of timebins yields $n_{drift} = 1.234 \cdot 620/32$ timebins $\approx 765/32$ timebins ≈ 23.9 timebins. This value can now be set

in the TRAP configuration to run a new simulation and verify the expected improvement. Figure 4.12 shows the Δd_y distribution (4.12a) and the efficiency (4.12b) after the setting of the corrected drift velocity. Clearly, the width of the Δd_y distribution has been considerably decreased, and the symmetry has been improved in both plots. For the efficiency, this means of course losing more tracklets than before; however, the loss is hardly relevant for particles with $p_\perp \geq 2$ GeV/c, which are of interest for the triggering, and can therefore be neglected. In summary, the setting of the correct drift velocity contributes significantly to the improvement of the local on-line tracking.

4.4 Position correction

After improving the deflection in the previous section, now we take a look at the transverse position y . As before, a shift distribution is extracted for the y position of the tracklets in comparison with the y position of the Monte Carlo track references. To be able to directly compare the y positions, the radial position of the track references must be propagated to the radial position of the tracklets, and the pad tilting must be accounted for when calculating the y position of the track references. This is performed in the off-line analysis task. The resulting distribution of the shift $\Delta y = \Delta y_{sim} - \Delta y_{MC}$ is shown in Figure 4.13.

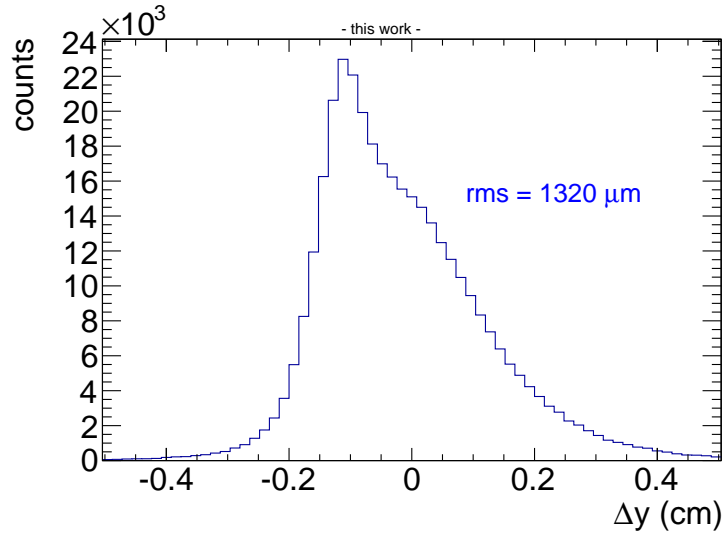
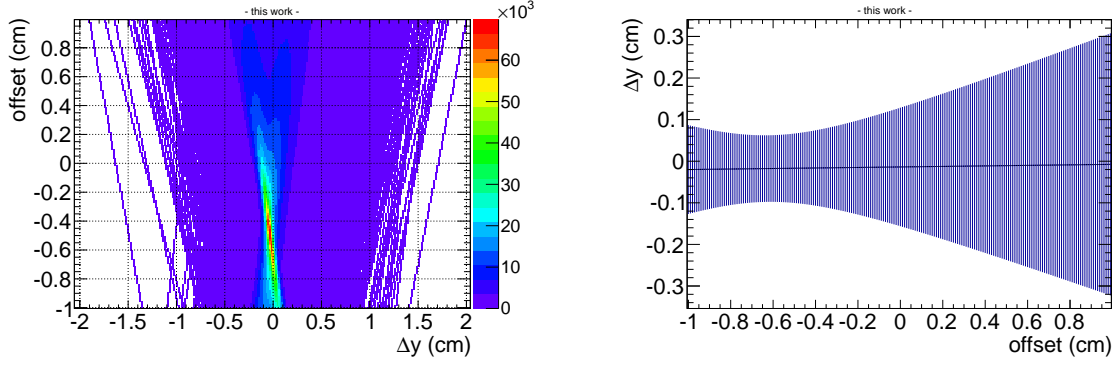


Figure 4.13: Distribution of the position shift $\Delta y = \Delta y_{sim} - \Delta y_{MC}$.

To explain the broad width of the distribution, the following must be taken into consideration: The radial position $x(t = 0)$ where the transverse position of the tracklets is determined is needed for the propagation of the MC track references. However, the function of the TRD geometry class used to extract the x position of the tracklets at $t=0$ returns a value which does not exactly correspond to the y position of the tracklets given by the tracklet word. This in turn means that the y position of the MC track references is determined at the wrong x position, resulting in the large shift of Δy as observed in Figure 4.13.

The x position of the tracklets can be corrected in a similar procedure as applied in Section 4.3 for the correction of the drift velocity: When propagating the Monte Carlo track references to the radial position of the tracklets, an additional offset is added to the x position of the tracklets and tuned to find the minimal width of the shift distribution. This allows to plot the position shift Δy as a function of the offset (Figure 4.14a) and to obtain a profile (Figure 4.14b). From the profile, a range of interest for the offset is determined, and shift distributions and their rms values are extracted from Figure 4.14a for each offset in the range. From the plotted rms values as a function of the offset (see Figure 4.15), the minimum and the corresponding offset are determined using a second degree polynomial fit.



(a) The position shift Δy is plotted depending on the offset.

(b) Profile obtained from left plot. The rms value of the shift distribution is smallest around -0.6 cm.

Figure 4.14: Determination of the offset.

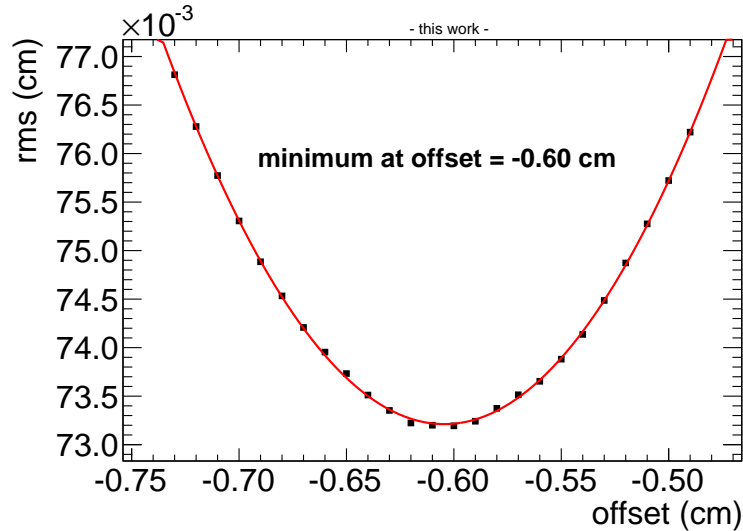


Figure 4.15: A second degree polynomial is used to fit the distribution of the rms values as a function of the offset. From the minimum, the correct offset is obtained.

The offset at the minimum is determined to be ~ -0.60 cm. This value could be set in the GTU to correct the x values of the tracklets during the global tracking. With the determined value for the offset, a corrected Δy distribution with a significantly reduced width can be obtained as shown in Figure 4.16.

Previously, the determination of the y position was determined at the radial position corresponding to timebin 0 (see Figure 3.2). This introduces another error in the shift distribution: Since this plane of reference is located slightly above the pad plane, the deflection is needed to propagate the tracklet to this position. However, the previous section has shown that the deflection is subject to corrections, which are only applied *after* the propagation of the tracklet y position. Therefore, the uncorrected deflection causes a deterioration of the y position due to the correlation of the two quantities.

A possible solution is to determine the transverse position of the tracklets at the radial position of the anode wire plane, thus decoupling the y position measurement from the deflection. By taking a look at the distribution of the total charge over the time in Figure 4.17, it becomes clear that the position of the anode wire plane, which corresponds to the peak in the beginning (see Section 2.3.1), is located somewhere around timebin 2. Although Figure 4.17 is taken from the ALICE logbook entry for Run

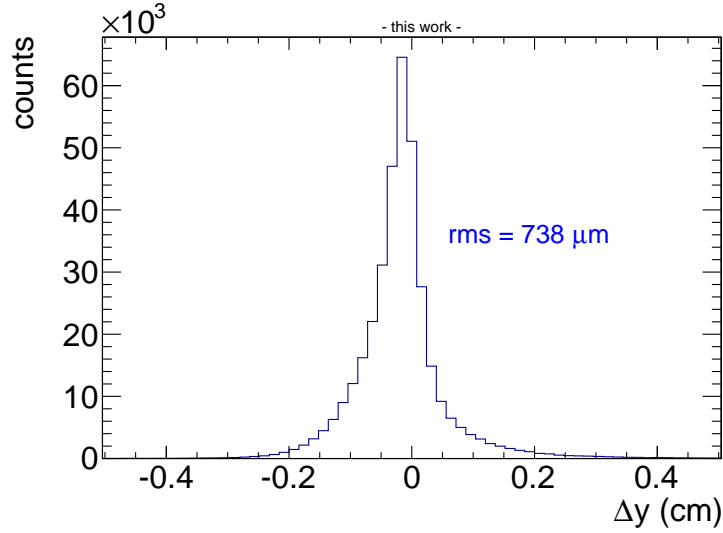


Figure 4.16: Δy distribution with the corrected offset. The width of the distribution could be significantly improved.

197388 in the data taking period LHC13f, and is therefore not directly applicable to the Monte Carlo productions used in this thesis, it motivates the introduction of a time offset t_0 to shift the reference plane of the y position down to the anode wires. This can be achieved by including t_0 in the tracklet calculation in the MCMs.

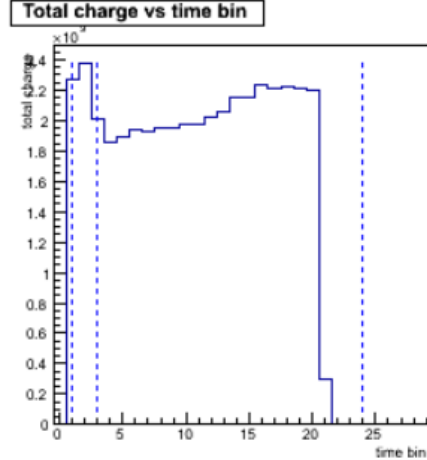


Figure 4.17: Distribution of the total charge over the time, taken from the ALICE logbook entry for Run 197388 in the data taking period LHC13f. The peak in the beginning corresponds to the position of the anode wire plane, and is used as a motivation for the setting of the time offset t_0 .

Since we want the time measurement relative to t_0 , the fit sums of Section 3.2.2 now have to be calculated for $t - t_0$ instead of t . This results in two additional terms in the numerator of the equation for y :

$$y = \frac{X^2 \cdot Y - X \cdot (XY) + t_0 \cdot N \cdot (XY) - t_0 \cdot X \cdot Y}{N \cdot X^2 - X \cdot X}.$$

The equation of the slope b , on the other hand, is unaffected by the time offset and remains unchanged. The additional terms are implemented in the `AliTRDmcmSim` class, and the time offset is configured in

the `AliTRDtrapConfig` class. With the value for t_0 set as 2 timebins in the TRAP configuration, a new simulation was produced to verify the expected improvement in the shift distribution. Subsequently, the same procedure as before is used to determine the optimal value for the offset in order to correct the tracklet x position. The obtained distribution is shown in Figure 4.18:

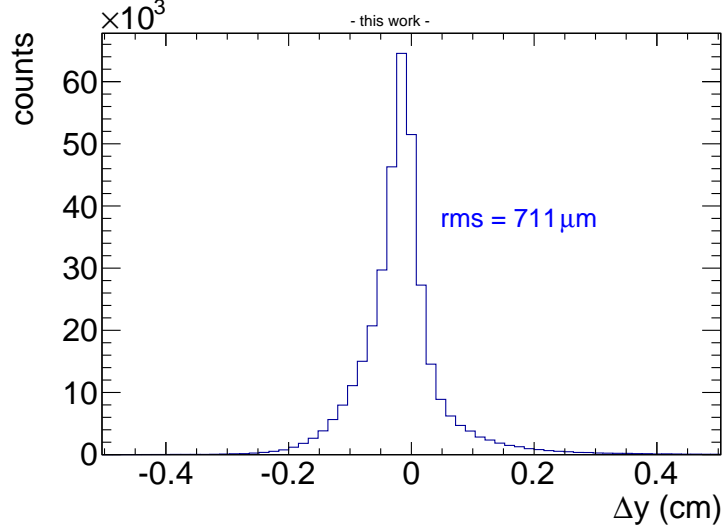


Figure 4.18: Distribution of the y shift with a time offset of $t_0 = 2$ timebins.

The width of the distribution could not be significantly improved compared to Figure 4.16. However, the setting of the time offset is not yet fully explored, and needs further testing and analysis to thoroughly judge its effect on the y position. One possibility could be to increase the precision of the setting of t_0 , so that not only integers could be set, and then to study the effect of using different time offsets around $t_0 = 2$ timebins.

4.5 Correction of mis-alignment

As the final part of the optimisation of the local on-line tracking, we take a look at a Monte Carlo simulation which includes the mis-alignment of the chambers. In Figure 4.19, the shift of the y position is shown for the different detector modules, numbered from 0 to 539. The mis-alignment causes offsets of up to 2 cm for some chambers. However, the difference in neighbouring chambers is small and the influence on the global tracking limited enough that the mis-alignment was neglected in Run 1 [8].

The values for the mis-alignment used in this MC production were extracted from measurements of the supermodules. For the simulation, a run from the data taking period in 2012 was used, when only 13 supermodules were included. For this reason, Figure 4.19 shows gaps corresponding to the supermodules that were installed in 2014, for which no run with alignment data is available yet². Still, the simulation can be used to test a procedure which adds a correction value to the transverse position in order to correct the mis-alignment in y direction, i.e.

$$y = y_0 + y_{corr}(\text{detector, ROB, MCM}).$$

Here, y_0 is the mis-aligned transverse position, whereas y_{corr} represents the corrective value. As indicated in the equation, the correction could be done chamber-wise (denominated by the variable detector as in Figure 4.19), once per read-out board, or individually for each MCM, making it feasible to implement it on the MCMs.

In this thesis, a chamber-wise correction is sufficient to demonstrate the improvement in the mis-alignment. In the first step, a Δy distribution is extracted for each chamber. A Gauss fit is then used to determine the offset from 0. Subsequently, a new variable y_{corr} is defined in the `AliTRDtrapConfig` class and added to the y position in the `AliTRDmcmSim` class. The results of this correction are shown

²as of February, 25

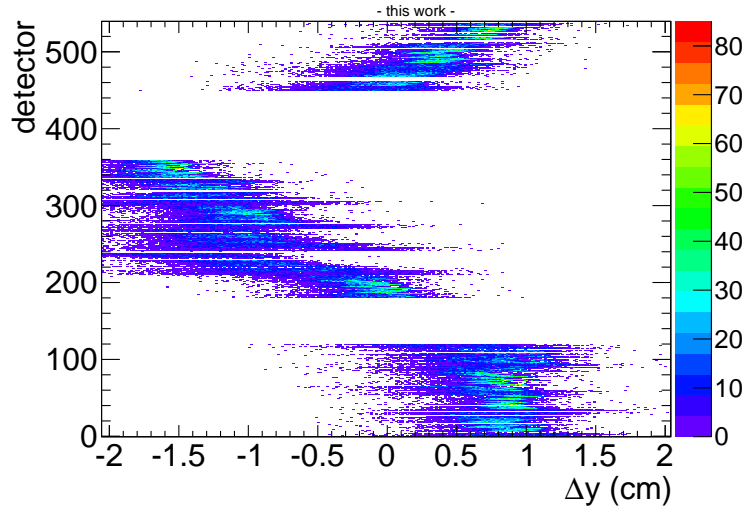


Figure 4.19: Position shift Δy depending on the chamber to illustrate the mis-alignment in y direction. The gaps inbetween are due to missing supermodules.

in Figure 4.20. The procedure proves to be quite successful, as the average value of the Δy distribution for every chamber has clearly been shifted to, or close to, 0. Still, the statistics provided for were quite low for some chambers, making a reasonable Gauss fit of the distributions difficult. This could be improved by producing a simulation with a larger number of events, which was not possible in the time frame of this thesis. Additionally, the mis-alignment due to rotation around the axes puts a limitation to the achievable results.

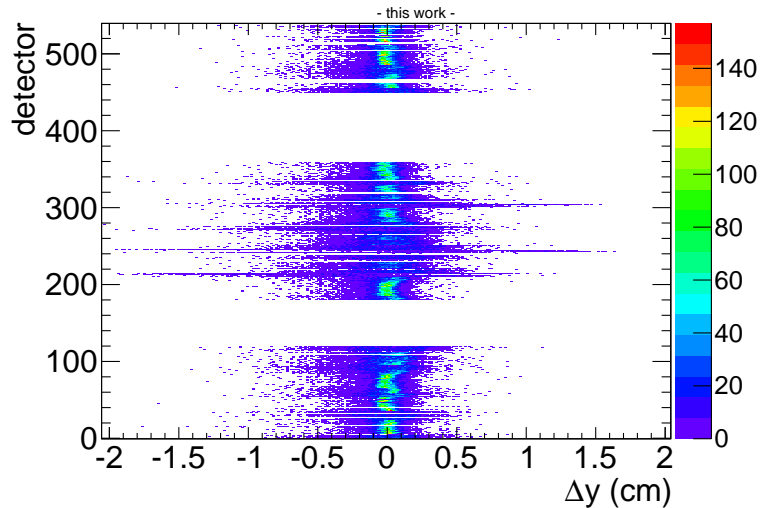
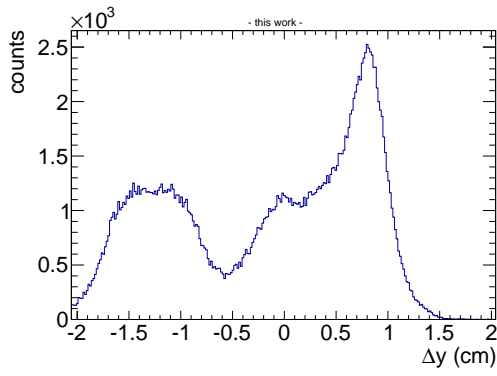
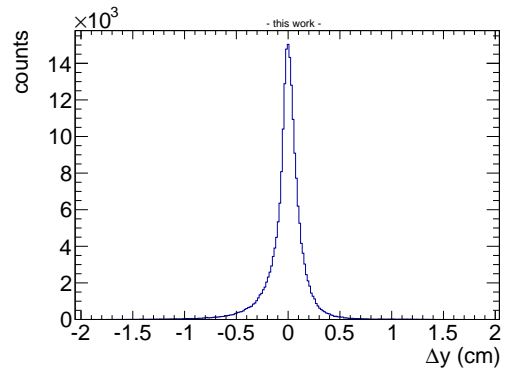


Figure 4.20: y shift for the detector chambers with corrected mis-alignment. The most probable values for the different chambers are clearly distributed around 0.

To further illustrate the improvement, Figure 4.21 shows the Δy distribution of all chambers combined before and after the mis-alignment correction. While the values are spread over almost the entire scale of -2 cm to 2 cm for the uncorrected mis-alignment in Figure 4.21a, a more Gaussian distribution with a reasonable width is obtained after the mis-alignment correction (see Figure 4.21b).



(a) Distribution of Δy for mis-aligned chambers.



(b) Distribution of Δy after the mis-alignment has been corrected.

Figure 4.21: Comparison of the Δy distributions to illustrate the mis-alignment correction

5 Summary and outlook

In this thesis, different optimisations of the local on-line tracking in the TRD have been studied. Also, the improvements were implemented. The optimisation was performed on the basis of Monte Carlo simulations for minimum bias pp collisions at $\sqrt{s} = 8$ TeV produced specifically for this purpose. A dedicated off-line analysis task was implemented to analyse the simulated data and verify the improvement made by the applied corrections.

Another important part of this thesis was the contribution to the commissioning of the TRD for Run 2. This included several trips to CERN to test the supermodules both prior to and after the installation in the experiment. The participation resulted in the successful restoration of connections to the front-end electronics as well as the repair of low voltage power supplies, thus contributing to the full read-out of the TRD.

As a first step to optimise the local on-line tracking, the number of tracklets belonging to one track reference pair was investigated. Tracklets can be found more than once due to the tracking algorithm used in the MCMs. As this deteriorates the PID, an algorithm was conceived to sort the tracklets with regard to their charge, select the one with the highest charge and discard the others. After testing this algorithm in the off-line analysis task, it was implemented in the `AliTRDmcmSim` class to test its functionality in the MCMs. Using this implementation, the number of tracklets found more than once could be successfully reduced from $\sim 40\%$ to only $\sim 7\%$. The remaining multiple tracklets are mainly caused by charge sharing across pad rows, which cannot be corrected in the local on-line tracking.

The next part was concerned with the improvement of the parameters needed for the straight-line fit, i.e. the transverse position with respect to the chamber centre and the deflection over the 3 cm drift length. These are important as they are needed for the global tracking in the GTU. To judge the quality of the tracklet position and deflection, shift distributions from comparisons with the position and deflection of the Monte Carlo track references were extracted.

The shift distribution of the deflection d_y could be significantly improved by using the drift velocity as an effective value to compensate the effect of the ion tails. Although the efficiency of the tracklets was slightly worsened in the process, the efficiency loss is not relevant for the range in p_\perp that is of interest for the triggering.

As a first step to correct the transverse position y , an offset to the alleged x position of the tracklets at $t=0$ was introduced in the propagation of the Monte Carlo track references. This allowed the track references to be shifted to the radial position where the y position of the tracklets was truly determined. By tuning the offset until the width of the shift distribution was minimized, the optimal offset value could be determined. In a second step, a time offset was added in the calculation of the fit sums in the `AliTRDmcmSim` class in order to shift the reference plane of the transverse position closer to the anode wire plane, thus decoupling the y position from the uncorrected deflection. Further study is needed to evaluate the influence of this correction on the y position.

Finally, we focused on the correction of the mis-alignment of the detector modules. Here, a method was tested to add a corrective value in the calculation of the transverse position on the MCMs in order to compensate for the mis-alignment. The improvement achieved by this method could be verified by extracting an average offset from 0 for each chamber, and subsequently subtracting it from the y position using the `AliTRDmcmSim` class. For an actual implementation on the MCMs, however, the alignment data from the supermodules would be needed, which is not available yet for the supermodules installed in 2014.

In conclusion, the local on-line tracking could be improved in various ways by implementing and testing different methods in Monte Carlo simulations. Consequently, the next step would be the actual integration of the methods into the FEE configuration and program, and thus to verify the settings, or further improve them, by using raw data from data taking with the detector.

References

- [1] K.A. Olive et al. (Particle Data Group). Review of Particle Physics. *Chin. Phys. C*, 38, 090001 (2014). URL: <http://pdg.lbl.gov/>.
- [2] Mark Thomson. *Modern Particle Physics*. Cambridge University Press, 2013.
- [3] Cern web page, February 2015. URL: <http://home.web.cern.ch/>.
- [4] Alice web page, February 2015. URL: <http://aliceinfo.cern.ch/>.
- [5] L. Evans und P. Bryant (editors). LHC Machine. *Jinst 3 S08001*, 2008. doi:10.1088/1748-0221/3/08/S08001.
- [6] B. Abelev et al. (ALICE Collaboration). Performance of the ALICE Experiment at the CERN LHC. *Int. J. Mod. Phys. A* 29 (2014) 1430044, 2014. arXiv:1402.4476 [nucl-ex]. doi:10.1142/S0217751X14300440.
- [7] CERN Communication Group. LHC: the guide (English version). CERN-Brochure-2009-003-Eng, 2009. URL: <http://cds.cern.ch/>.
- [8] J. Klein. *Jet Physics with A Large Ion Collider Experiment at the Large Hadron Collider*. Doctoral thesis, University of Heidelberg, 2014.
- [9] P. Cortese et al. (ALICE Collaboration). ALICE Technical Design Report of the Transition Radiation Detector. Technical Design Report ALICE. CERN, Geneva, 2001.
- [10] K. Aamodt et al. (ALICE Collaboration). The ALICE experiment at the CERN LHC. *JINST 3 S08002*, 2008. doi:10.1088/1748-0221/3/08/S08002.
- [11] J. de Cuveland. *Entwicklung der globalen Spurrekonstruktionseinheit für den ALICE-Übergangsstrahlungsdetektor am LHC (CERN)*. Diploma thesis, University of Heidelberg, 2003.
- [12] J. Klein (ALICE Collaboration). Triggering with the ALICE TRD. *Nucl.Instrum.Meth., A706:23-28*, 2013. arXiv:1112.5110 [nucl-ex]. doi:10.1016/j.nima.2012.05.011.
- [13] M. Walter. *Performance of Online Tracklet Reconstruction with the ALICE TRD*. Diploma thesis, University of Münster, 2010.
- [14] N. Wahl. *Performance of the local on-line Tracking and of a track-based Jet Trigger Algorithm for the ALICE TRD on the Basis of Monte-Carlo simulations*. Bachelor's thesis, University of Heidelberg, 2011.
- [15] Definition of the ALICE Coordinate System and Basic Rules for Sub-detector Components Numbering, February 2015. URL: <https://edms.cern.ch/file/406391/2/ALICE-INT-2003-038.pdf>.
- [16] The ALICE Off-line Project, February 2015. URL: <http://aliweb.cern.ch/Offline/>.

Erklärung

Ich versichere, dass ich diese Arbeit selbstständig verfasst und keine anderen als die angegebenen Quellen und Hilfsmittel benutzt habe.

Heidelberg, den 25.02.2015,